Optimizing Josephson-ring-modulator-based Josephson parametric amplifiers via full Hamiltonian control

Chenxu Liu, Tzu-Chiao Chien ⬭, Michael Hatridge, and David Pekker
Department of Physics and Astronomy, University of Pittsburgh
and Pittsburgh Quantum Institute, Pittsburgh, Pennsylvania 15260, USA

Josephson parametric amplifiers (JPA) are nonlinear devices that are used for quantum sensing and qubit readout in the microwave regime. While JPAs regularly operate near the quantum limit, their gain saturates for very small (few-photon) input power. In a previous work, we showed that the saturation power of JPAs is not limited by pump depletion, but instead by the fourth-order nonlinearity of Josephson junctions, the nonlinear circuit elements that enables amplification in JPAs. Here, we present a systematic study of the nonlinearities in JPAs, show which nonlinearities limit the saturation power, and present a strategy for optimizing the circuit parameters for achieving the best possible JPA. For concreteness, we focus on JPAs that are constructed around a Josephson ring modulator (JRM). We show that by tuning the external and shunt inductors, we should be able to take the best experimentally available JPAs and improve their saturation power by ≈ 15 dB. Finally, we argue that our methods and qualitative results are applicable to a broad range of cavity-based JPAs.

I. INTRODUCTION

Amplification is a key element in quantum sensing and quantum information processing. For example, readout of superconducting qubits requires a microwave amplifier that adds as little noise to the signal as possible [1], ideally approaching the quantum limit [2–4]. Recently, low-noise parametric amplifiers powered by the nonlinearity of Josephson junctions have been realized and are in regular use in superconducting quantum information experiments [5–14].

To evaluate the performance of a practical parametric amplifier, there are three aspects that are equally important: (1) added noise at the quantum limit [4,8–11,15], (2) broadband amplification [15–19], and (3) high saturation power [9,20–26], i.e., the ability to maintain the desired gain for a large input signal power [27]. The last requirement has been especially hard to achieve in Josephson parametric amplifiers and will be the focus of this paper.

In previous works on Josephson parametric amplifiers, it was assumed that saturation power is limited by pump depletion [9,20–22,26]. This is a natural explanation, as the amplifier gain is a very sensitive function of the flux of the applied pump photons. Thus, as the input power is increased and more pump photons are converted to signal photons, the gain falls. However, in Refs. [23–25,28] it was pointed out that the fourth-order nonlinear couplings (i.e., the Kerr terms), inherent in Josephson-junction-based amplifiers, can also limit the saturation power. These terms induce a shift in the mode frequencies of the amplifier as a function of signal power, which can cause the amplifier to either decrease or increase its gain. Thus, we adopt the definition of saturation power as the lowest input power that causes the amplifier's gain to either increase or decrease by 1 dB, which we abbreviate as $P_{\pm 1 \text{dB}}$.

In this paper, we address the question: For a given device, does pump depletion, Kerr terms, or higher order nonlinearities limit the saturation power $P_{\pm 1 \text{dB}}$? How do we tame these limitations to optimize the device by maximizing $P_{\pm 1 \text{dB}}$? Our analysis and results are generally applicable for all amplifiers based on third-order couplings, including JPAs based on superconducting nonlinear asymmetric inductive elements (SNAILs) [25,29–31], flux-pumped superconducting quantum interference devices (SQUIDs) [7,32–35], and the Josephson parametric converters (JPCs) [8,9,21,24,36]. These techniques we develop may also be of use in the simulation of non-cavity-based amplifiers, such as the traveling-wave parametric amplifier (TWPA) [37–39].

In the JPC, three microwave modes (a, b, and c) are coupled via a ring of four Josephson junctions [the so-called Josephson ring modulator (JRM); see Fig. 2(b) shaded part, for example]. A third-order coupling ($g_3 \varphi_a \varphi_b \varphi_c$) between the fluxes ($\varphi_i$) of three microwave modes is obtained by applying a static magnetic flux to the JRM ring. Phase-preserving gain is obtained by pumping one mode (typically c) far off resonance at the sum frequency of the other two (a and b), with the gain amplitude being controlled by the strength of the pump drive.

We now discuss the main results of our investigation, which are summarized in Fig. 1. Previously, descriptions of JPC's relied on expanding the nonlinear couplings between the three microwave modes in a power series of cross- and self-couplings. The power series was truncated at the lowest possible order, typically fourth (i.e., corresponding to the cross- and self-Kerr terms) [9,11,17,24]. In the present paper, we compare these power series expansions with the exact numerical solutions in the framework of semiclassic input-output theory. Our first main finding is that there is indeed a sweet spot for operating a JPA [see Fig. 1(a)], at which $P_{\pm 1 \text{dB}}$ is maximized. The sweet spot appears for moderate values of
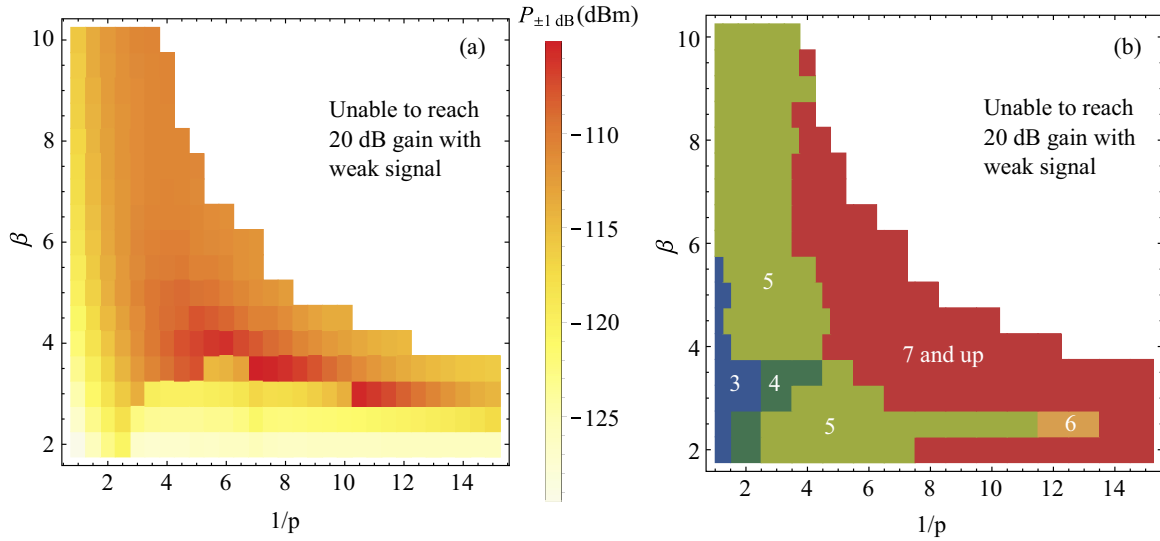
FIG. 1. The saturation power for the JRM-based Josephson parametric amplifier with various JRM inductance ratio β and participation ratio p is shown in panel (a). The amplifier has a sweet spot, in which saturation power is maximal, in the low-β and intermediate-p regime. Optimizing β and p, we find saturation power of $P_{\pm 1 \text{ dB}} \sim -104.8$ dB m at $\beta \approx 3.5$, $1/p \approx 7.0$. For small p and large β, the amplifier is not able to reach the desired reflection gain (of 20 dB); this region is labeled in white. In the intermediate-p regime ($1/p \sim 4$ to 10), as we lower β, the saturation power first increases, hits the sweet spot, and then abruptly drops. To understand this behavior, we refer to Fig. 9(a), which shows that the gain at large signal powers tends to increase as β decreases. This trend is at first beneficial to the amplifier, as the gain vs signal power curve flattens out. However, at even lower β, the gain tends to increase with signal power (a feature that we call the "shark fin"), resulting in the amplifier saturating to 21 dB [see Fig. 9(a), $\beta = 3$ curve] and hence the saturation power abruptly decreasing. The sweet spot of the saturation power is located at the edge of the this "reflection gain boost" regime. In panel (b), we show the minimum truncation order needed to converge small-signal reflection gain of the amplifier to 20 ± 0.3 dB. In our main text, we show that the convergence order of small-signal reflection gain gives a good prediction on the convergence order of the saturation power [see Figs. 9(b) and 9(c)]. In the small-β, large-p corner, the third-order truncation is enough to make the time solver converge to the desired 20 dB reflection gain. While as we decrease the participation ratio, increasingly higher orders are needed to converge the truncated theory, which shows that the full-order simulation is needed to predict the performance of the amplifier near the sweet spot.

the two circuit parameters: participation ratios $p \sim 1/7$ and shunt inductance ($\beta = L_J/L_{in} \sim 3.5$, where L_{in} is the shunt inductance, $L_J = \varphi_0/I_0$ is the Josephson inductance, $\varphi_0 = \hbar/2e$ is the reduced flux quantum, and I_0 is the Josephson junction critical current). Our second main finding is that in the vicinity of the sweet spot nonlinear terms up to at least seventh order are comparable in magnitude and hence truncating the power series description at fourth order is invalid; see Fig. 1(b). The second main result can be interpreted from two complementary perspectives. First, the sweet spot corresponds to high pump powers and hence the energy of Josephson junctions cannot be modeled by a harmonic potential anymore. Second, different orders of the power series expansion have either a positive or a negative effect on the gain as a function of signal power; when the magnitudes of terms at different orders are comparable, the terms cancel each other, resulting in a boost of $P_{\pm 1\text{dB}}$. We hypothesize that the second main finding is a generic feature for Josephson-junction-based parametric amplifiers.

Before moving to a detailed development of our theory, we provide a summary of the key steps of our investigation and outline the structure of our paper.

We begin by noting that in addition to the above-mentioned parameters p and β, the magnetic flux through the JRM $\varphi_{ext} = (2\pi/\varphi_0)\Phi_{ext}$ is another important control parameter. For conventional JRMs [8,9], at nonzero values of applied flux there are nonzero cross- and self-coupling at all orders

(fourth, fifth, etc.). However, we have recently realized that a linearly shunted variant of the JRM [11,17] can null all even-order couplings at a special flux bias point ($\varphi_{ext} = 2\pi$), which we call the Kerr nulling point. The same nulling is also observed in SNAIL-based devices [29]. In the context of a JPC with participation ratio $p < 1$, even couplings come back but remain much smaller than at generic values of φ_{ext}. Therefore, throughout this paper, we focus on φ_{ext} at or in the vicinity of the Kerr nulling point.

We calculate the saturation power using semiclassical equations of motion for the microwave modes, which are derived using input-output theory from the Lagrangian for a lumped-circuit model of the JPA. When we consider higher than third-order couplings, these equations are not generally analytically solvable. To analyze the saturation power for a given set of parameters, we compare numerical integration of the full nonlinear equations to solutions of various, artificially truncated versions of the equations obtained using both numerical integration and perturbation theory. We begin by investigating the effects of pump depletion. To do so, we analyze the dynamics of all the modes with interactions truncated at third order. Using classical perturbation theory to eliminate the dynamics of the pump mode (c), we find, in contradiction with the basic understanding of pump depletion, that the first corrections are a complex fourth-order cross-Kerr coupling between modes a and b, and an associated two-photon loss process in which pairs of a and b photons decay into the

c mode, that effectively *increase* the pump strength. The dynamically generated Kerr terms act similarly to the intrinsic Kerr terms, including giving rise to saturation to higher gain when the pump mode frequency is positively detuned from the sum frequency. Further, in the shunted JRM, we can partially cancel the real part of the dynamically generated Kerr by tuning the applied flux near the Kerr nulling point so as to generate an opposite-sign intrinsic Kerr. Thus, the presence of judicious intrinsic Kerr can be a virtue, and the ultimate pump depletion limit is set by the imaginary Kerr and two-photon loss. Increasing the β value of the JRM reduces these effects and increase the JPCs saturation power. Away from the nulling point, these depletion effects are overwhelmed by the intrinsic Kerr effects, and the device is Kerr limited, in agreement with our previous results.

Next, we perform calculations with full nonlinearity and find that saturation power stops increasing at high β. We find that this is primarily due to certain fifth-order terms of the form $(\varphi_a^2 + \varphi_b^2)\varphi_a\varphi_b\varphi_c$. These terms modulate the effective parametric coupling strength as a function of the input signal power, thus shifting the amplifier away from the desired gain by increasing the effective parametric coupling (in fact, throughout this work we failed to identify a scenario in which the amplifier runs out of pump power).

To suppress the strength of these terms relative to the desired third-order coupling, we introduce an additional control knob by adding outer linear inductors L_{out} in series with the JRM. The participation ratio $p = L_{\text{JRM}}/(2L_{\text{out}} + L_{\text{JRM}})$, where L_{JRM} is the effective inductance of the JRM, controls what fraction of the mode power is carried by the JRM. Decreasing p results in the suppression of all coupling terms; however, the higher order coupling terms decrease faster than the lower order ones. Thus, if the saturation power is limited by intrinsic fifth-order terms, we can increase the saturation power by decreasing the participation ratio p. We remark that as the pump power is increased, the cross-coupling terms result in a shift of the JPA frequencies that must be compensated, which we do for each value of p and β. Tuning both p and β, we can find a sweet spot for the operation of the JPC, as discussed above.

In general, the mode frequencies shift with applied pump power. This, combined with the fact that JPAs can function with pump detunings comparable to the bandwidth of the resonators on which they are based, makes comparing theory and experiment very complicated. For concreteness, our simulations vary the applied pump and signal frequencies to identify the bias condition which requires minimum applied pump power to achieve 20 dB of gain. These points can be readily identified in experiments [24]. However, there has been a recent observation in SNAIL-based JPAs that deliberate pump detuning can additionally enhance device performance [30] and serve as an *in situ* control to complement the Hamiltonian engineering we discuss in this work.

This paper is organized as follows. In Sec. II, we focus on the closed model of JPA circuit (without input-output ports). We start by reviewing the basic theory of circuits with inductors, capacitors, and Josephson junctions in Subsec. II A. In Subsec. II B, we include the external shunted capacitors with JRM and present the normal modes of the JPA circuit model using Lagrangian dynamics. In Sec. III, we further include

the input-output ports into the circuit model of the JPA and construct the equations of motion to describe the dynamics of the circuit. In Sec. IV, we investigate the limitation on the saturation power of the JPA without external series inductors. Specifically, we analyze the third-order theory using both numerical and perturbative approaches in Sec. IV C. We compare these results with the effect of Kerr nonlinearities in Sec. IV D and identify the dynamically generated Kerr terms and the two-photon loss processes. Intrinsic fifth- and higher order nonlinear couplings are investigated in Sec. IV E. We put these results together in Sec. IV A and identify which effect is responsible for limiting the saturation power in different parametric regimes. In Sec. V, we consider the consequence of the series inductors outside of it. We show that the series inductors, which suppress the participation ratio of the JRM, can be used to improve the dynamic range of the JRM. We discuss how to optimize the saturation power of the JPA, taking into account both series inductors and full nonlinearities in Sec. VI. In Sec. VII, we further explore how the saturation power is affected by the magnetic field bias, the modes' decay rates, and stray inductors in series of the Josephson junction in JRM loop. We provide an outlook on the performance of Josephson-junction-based amplifiers in Sec. VIII.

II. EQUATIONS OF MOTION FOR CIRCUITS MADE OF INDUCTORS, CAPACITORS, AND JOSEPHSON JUNCTIONS

In this section, we review the theory of lumped circuits elements. We start from the Lagrangian treatment of single circuit elements in Subsec. II A. Then in Subsec. II B, we work on the JRM and the closed JPA circuit model and solved the normal mode profiles of the JRM.

A. Lagrangian description of linear inductance, Josephson junctions, and capacitors

The equations of motion (EOM) that describe the dynamics of a circuit with Josephson junctions, inductors, and capacitors can be derived using the formalism of Lagrangian dynamics, which naturally leads to Kirchhoff's law. We use the dimensionless flux on each node of the circuit, $\varphi_j(t) = \frac{1}{\phi_0}\int_{-\infty}^{t} V_j(t')dt'$, as the set of generalized coordinates. The Lagrangian $\mathcal{L}[\{\varphi_j, \dot{\varphi}_j\}]$ is defined as

$$\mathcal{L} = T[\{\dot{\varphi}_j\}] - U[\{\varphi_j\}], \tag{1}$$

where T is the kinetic energy associated with the capacitors and U is the potential energy associated with the inductors and the Josephson junctions. Using Fig. 2(a) to define the nodes and current direction for each type of circuit element, we observe that each capacitor contributes

$$E_C = \frac{C}{2}\phi_0^2(\dot{\varphi}_1 - \dot{\varphi}_2)^2 \tag{2}$$

to $T[\{\dot{\varphi}_j\}]$, while each inductor and each Josephson junction contributes

$$E_L = \frac{\phi_0^2}{2L}(\varphi_2 - \varphi_1)^2, \tag{3}$$

$$E_{\text{J}} = -\phi_0 i_c \cos(\varphi_2 - \varphi_1), \tag{4}$$
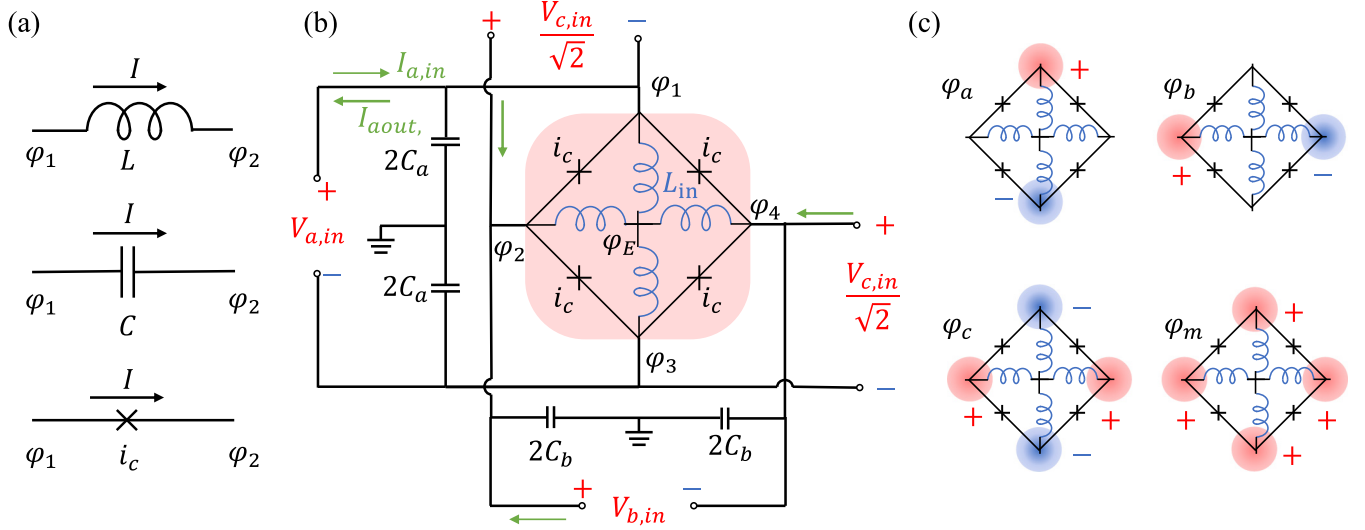
(a)

(b)

(c)

FIG. 2. In panel (a), we show the typical circuit elements that we will focus on in this paper, a linear inductor with inductance L, a capacitor with capacitance C, and a Josephson junction with critical current i_c. The node phase and the convention for the current is labeled on each element drawings. The circuit model for the JRM-based JPA circuit is shown in panel (b). The circuit model for a linear inductance shunted Josephson ring modulator (JRM) is shaded in red. We connected the linear inductance shunted JRM with the capacitors and the input-output ports. We assume the normal modes are symmetrically driven by the ports. For the port corresponding to mode φ_a, we use the green arrows to show the input and output (reflected) current flow direction. For b mode, we only use the green arrow to show the flow direction of the input current. The connection of the c port is not shown in the plot. The c port also drives the corresponding mode profile symmetrically. The corresponding normal modes, including three nontrivial modes φ_a, φ_b, and φ_c and one trivial mode φ_m are shown in panel (c).

to $U[\{\varphi_j\}]$, where i_c is the critical current of the Josephson junctions. The current across a capacitor is $-\frac{1}{\phi_0}(\delta E_C/\delta\varphi_1) = \frac{1}{\phi_0}(\delta E_C/\delta\varphi_2)$, while the current across an inductor is $\frac{1}{\phi_0}(\delta E_L/\delta\varphi_1) = -\frac{1}{\phi_0}(\delta E_L/\delta\varphi_2)$ and across a Josephson junction $\frac{1}{\phi_0}(\delta E_J/\delta\varphi_1) = -\frac{1}{\phi_0}(\delta E_J/\delta\varphi_2)$. Using the Lagrangian $\mathcal{L}$ of the circuit elements, the current that flows out of each node of the circuit is $J_j = -\frac{1}{\phi_0}(\delta\mathcal{L}/\delta\varphi_j)$. To obtain the equations of motion (EOMs) we extremize the action by setting $J_j = 0$, which corresponds to enforcing Kirchhoff's law.

Next, we apply the Lagrangian formalism to derive the potential energy of the linear-inductor-shunted JRM, the key component at the heart of the JPA, shown in Fig. 2(b), which is shaded in red. The potential energy of the JRM circuit [40] is

$$E_{\mathrm{JRM}} = \frac{\phi_0^2}{2L_{\mathrm{in}}} \sum_{j=1}^{4} (\varphi_j - \varphi_E)^2$$

$$- \phi_0 i_c \sum_{i=1}^{4} \cos\left[\varphi_{i+1} - \varphi_i - \frac{\varphi_{\mathrm{ext}}}{4}\right], \quad (5)$$

where φ_j's are the phases of the superconductors on the nodes [see Fig. 2(b)] and we adapt the convention that $\varphi_5 = \varphi_1$ for the summation. The external magnetic flux though the JRM circuit Φ_{ext} controls the parameter $\varphi_{\mathrm{ext}} = \Phi_{\mathrm{ext}}/\phi_0$. Applying Kirchhoff's law to node E, we obtain $\varphi_E = \frac{1}{4}(\varphi_1 + \varphi_2 + \varphi_3 + \varphi_4)$.

B. Normal modes of the Josephson parametric amplifier

In this sebsection, we focus on the equations of motion of the closed-circuit model of the JPA (i.e., ignore the input-

output ports) and analyze the normal mode profile of the JPA circuit (see Fig. 2(b), but without input ports).

The potential energy of the shunted JRM was derived in the previous subsection; see Eq. (5). The kinetic energy associated with the capacitors [Fig. 2(b)], Eq. (2), is

$$E_c = \phi_0^2 \big(C_a\dot{\varphi_1}^2 + C_b\dot{\varphi_2}^2 + C_a\dot{\varphi_3}^2 + C_b\dot{\varphi_4}^2\big), \quad (6)$$

which gives the Lagrangian $\mathcal{L} = E_c - E_{\mathrm{JRM}}$. The EOM of this closed circuit can be constructed using Lagrange's equation, e.g., for a node flux φ_j,

$$2C_j\ddot{\varphi_j} + \frac{1}{L_{\mathrm{in}}}(\varphi_j - \varphi_E) + \frac{1}{L_J}\left[\sin\left(\varphi_j - \varphi_{j+1} + \frac{\varphi_{\mathrm{ext}}}{4}\right)\right.$$

$$\left. - \sin\left(\varphi_{j-1} - \varphi_j + \frac{\varphi_{\mathrm{ext}}}{4}\right)\right] = 0, \quad (7)$$

where φ_j is the node phases, $j = 1, 2, 3, 4$, and we use the index convention that $\varphi_0 = \varphi_4$, $\varphi_5 = \varphi_1$. According to the Fig. 2(b), the node capacitance are $C_1 = C_3 = C_a$ and $C_2 = C_4 = C_b$. The Josephson inductance $L_J = \phi_0/i_c$.

To analyze the normal modes of the circuit, we assume we have chosen suitable values for the parameters so that the ground state of the circuit is $\varphi_1 = \varphi_2 = \varphi_3 = \varphi_4 = 0$, and expand in small oscillations to obtain a linearized set of EOMs around the ground state. The corresponding normal coordinates, which we denote as $[\varphi_M]$ in vector form, are related to the node fluxes via $[\varphi] = [\mathcal{A}][\varphi_M]$, where transformation matrix $[\mathcal{A}]$ is

$$[\mathcal{A}] = \begin{pmatrix} 1 & \frac{1}{2} & 0 & -\frac{C_b}{(C_a+C_b)} \\ 1 & 0 & \frac{1}{2} & \frac{C_a}{(C_a+C_b)} \\ 1 & -\frac{1}{2} & 0 & -\frac{C_b}{(C_a+C_b)} \\ 1 & 0 & -\frac{1}{2} & \frac{C_a}{(C_a+C_b)} \end{pmatrix}, \quad (8)$$

and the flux coordinates vectors are defined as $[\varphi] = (\varphi_1, \varphi_2, \varphi_3, \varphi_4)^\mathsf{T}$ and $[\varphi_M] = (\varphi_m, \varphi_a, \varphi_b, \varphi_c)^\mathsf{T}$. Inverting this transformation, we obtain the expression for the normal modes in terms of the node fluxes,

$$\varphi_a = \varphi_1 - \varphi_3, \tag{9a}$$

$$\varphi_b = \varphi_2 - \varphi_4, \tag{9b}$$

$$\varphi_c = -\frac{1}{2}(\varphi_1 + \varphi_3 - \varphi_2 - \varphi_4) \tag{9c}$$

$$\varphi_m = \frac{C_a}{2(C_a + C_b)}\left(\varphi_1 + \frac{C_b}{C_a}\varphi_2 + \varphi_3 + \frac{C_b}{C_a}\varphi_4\right). \tag{9d}$$

The profiles for the normal modes, φ_a, φ_b, φ_c, and φ_m are sketched in Fig. 2(c). The normal mode φ_m has zero frequency and it is not coupled with any of the other three modes [see Eq. (11)]. Therefore, φ_m is a trivial mode, which can be safely ignored in our following discussion. The corresponding frequencies for the other three nontrivial modes are

$$\omega_a^2 = \frac{L_\mathrm{J} + 2L_\mathrm{in}\cos\left(\frac{\varphi_\mathrm{ext}}{4}\right)}{2C_a L_\mathrm{in} L_\mathrm{J}}, \tag{10a}$$

$$\omega_b^2 = \frac{L_\mathrm{J} + 2L_\mathrm{in}\cos\left(\frac{\varphi_\mathrm{ext}}{4}\right)}{2C_b L_\mathrm{in} L_\mathrm{J}}, \tag{10b}$$

$$\omega_c^2 = \frac{C_a + C_b}{C_a C_b}\frac{L_\mathrm{J} + 4L_\mathrm{in}\cos\left(\frac{\varphi_\mathrm{ext}}{4}\right)}{4L_\mathrm{in} L_\mathrm{J}}. \tag{10c}$$

With the coordinate transformation given by the model matrix $[\mathcal{A}]$ [see Eq. (8)], we can rewrite the potential energy of the JPA (the energy of JRM circuit) using the normal modes φ_a, φ_b, and φ_c, as

$$\begin{aligned}
E_\mathrm{JRM} = -4E_\mathrm{J}\Big[&\cos\left(\frac{\varphi_a}{2}\right)\cos\left(\frac{\varphi_b}{2}\right)\cos(\varphi_c)\cos\left(\frac{\varphi_\mathrm{ext}}{4}\right) \\
&+ \sin\left(\frac{\varphi_a}{2}\right)\sin\left(\frac{\varphi_b}{2}\right)\sin(\varphi_c)\sin\left(\frac{\varphi_\mathrm{ext}}{4}\right)\Big] \\
&+ \frac{\phi_0^2}{4L_\mathrm{in}}(\varphi_a^2 + \varphi_b^2 + 2\varphi_c^2),
\end{aligned} \tag{11}$$

where $E_\mathrm{J} = \phi_0 i_c$ is the Josephson energy.

We observe from Eq. (11) that the four Josephson junctions on the outer arms of the JRM provide nonlinear couplings between the normal modes of the circuit. Assuming that the ground state of the circuit is $\varphi_a = \varphi_b = \varphi_c = 0$, and it is stable as we tune the external magnetic flux bias, we can expand the nonlinear coupling terms around the ground state as

$$\begin{aligned}
E_\mathrm{JRM} \sim &\left[\frac{\phi_0^2}{4L_\mathrm{in}} + \frac{E_\mathrm{J}}{2}\cos\left(\frac{\varphi_\mathrm{ext}}{4}\right)\right](\varphi_a^2 + \varphi_b^2) \\
&+ \left[\frac{\phi_0^2}{2L_\mathrm{in}} + 2E_\mathrm{J}\cos\left(\frac{\varphi_\mathrm{ext}}{4}\right)\right]\varphi_c^2 - E_\mathrm{J}\sin\left(\frac{\varphi_\mathrm{ext}}{4}\right)\varphi_a\varphi_b\varphi_c \\
&- \frac{1}{96}E_\mathrm{J}\cos\left(\frac{\varphi_\mathrm{ext}}{4}\right)(\varphi_a^4 + \varphi_b^4 + 16\varphi_c^4) \\
&+ \frac{1}{16}E_\mathrm{J}\cos\left(\frac{\varphi_\mathrm{ext}}{4}\right)(\varphi_a^2\varphi_b^2 + 4\varphi_a^2\varphi_c^2 + 4\varphi_b^2\varphi_c^2) + \cdots.
\end{aligned} \tag{12}$$

Because of the parity of the cosine and sine functions, the cosine terms in Eq. (11) contribute the even-order coupling terms while the sine terms contribute the odd-order coupling terms. The nonlinear couplings are controlled by the external magnetic flux bias φ_ext. The third-order nonlinear coupling is the desired term for a nondegenerate Josephson parametric amplifier, while all the higher order couplings are unwanted. The Kerr nulling point [17,29] is achieved by setting the external magnetic flux to $\varphi_\mathrm{ext} = 2\pi$ (and assuming that the ground state $\varphi_a = \varphi_b = \varphi_c = 0$ remains stable), and we find that all the even-order nonlinear couplings are turned off.

III. INPUT-OUTPUT THEORY OF THE JOSEPHSON PARAMETRIC AMPLIFIER

The linear-inductor shunted JRM described in the previous section is the core elements of the Josephson parametric amplifier. In order to build the JPA, we add input-output lines and external parallel capacitors to the JRM; see Fig. 2(b). In Sec. V, we will extend the description of the JPA by adding stray and series inductors to the JRM.

In order to fully model the JPA, we need to describe the input-output properties of the JPA circuit. In Subsec. III A, we introduce input-output theory and apply it to the problem of modeling drive and response of the JPA. In Subsec. III B, we present the full nonlinear equations of motion that describe the JPA circuit.

A. Input-output relation for the Josephson parametric amplifier

To solve the full dynamics of the JPA with amplification process, we need to be able to describe the microwave signals that are sent into and extracted (either reflected or transmitted) from the circuit. Therefore, we need to connect the input-output ports to the JPA circuit and include the description of them in the EOMs.

To simplify the problem, we assume that the drives perfectly match the profiles of the corresponding normal modes, as shown schematically for modes a and b in Fig. 2(a). Take mode a as an example. We send in a microwave signal with the amplitude of the voltage $V_{a,\mathrm{in}} = \phi_0\dot{\varphi}_{a,\mathrm{in}}$ into the port for this mode. The corresponding current flow from the transmission line to the amplifier is $I_{a,in} = \frac{V_{a,in}}{Z_a}$, where Z_a is the impedance of the transmission line. The voltages applied to nodes 1 and 3 are $V_1 = \frac{\phi_0}{2}\dot{\varphi}_{a,\mathrm{in}}$ and $V_3 = -\frac{\phi_0}{2}\dot{\varphi}_{a,\mathrm{in}}$, respectively, while the output microwave signal has output voltage amplitude $V_{a,\mathrm{out}} = \phi_0\dot{\varphi}_{a,\mathrm{out}}$ and the output current is $I_{a,\mathrm{out}} = \frac{V_{a,\mathrm{out}}}{Z_a}$.

At the nodes which connect to the transmission line, e.g., nodes 1 and 3 for a mode, the voltage and current should be single-valued. This requirement induces an input-output condition

$$\begin{aligned}
V_{a,\mathrm{in}} + V_{a,\mathrm{out}} &= V_a = V_1 - V_3, \\
I_{a,\mathrm{in}} - I_{a,\mathrm{out}} &= I_{1,a} = -I_{3,a},
\end{aligned} \tag{13}$$

where $I_{1,a}$ ($I_{3,a}$) is the net current flow into node 1 (3) of the amplifier from the port. Because the output signals should be determined by the input signals, we eliminate the output variables from the input-output relation so that it can be combined with the current relation inside the JRM to construct

the EOMs for the open circuit model

$$I_{1,a} = -I_{3,a} = \frac{2V_{a,\text{in}}}{Z_a} - \frac{\phi_0(\dot{\varphi}_1 - \dot{\varphi}_3)}{Z_a}. \tag{14}$$

Given the the drives (inputs), we can solve for the mode fluxes using the EOMs, and then obtain the outputs using the input-output relations. For example, the output voltage on port a is determined by

$$V_{a,\text{out}} = \phi_0(\dot{\varphi}_1 - \dot{\varphi}_3) - V_{a,\text{in}}. \tag{15}$$

In the remainder of this paper, we focus on the reflection gain of the JPA which is obtained from a phase-preserving amplification process. The input signal to be amplified by the JPA is a single-frequency tone. The amplified output is the reflected signal at the same frequency. Using the Josephson relation relating voltage and flux, we observe that the reflected voltage gain is equal to the reflected flux gain. Therefore, we use the input-output relation for the mode flux; e.g., for port a we have

$$\varphi_{a,\text{out}} = \varphi_1 - \varphi_3 - \varphi_{a,\text{in}}. \tag{16}$$

The analyses of input-output ports for modes b and c are similar. For b port, we have

$$I_{2,b} = -I_{4,b} = \frac{2V_{b,\text{in}}}{Z_b} - \frac{\phi_0(\dot{\varphi}_2 - \dot{\varphi}_4)}{Z_b}, \tag{17a}$$

$$V_{b,\text{out}} = \phi_0(\dot{\varphi}_2 - \dot{\varphi}_4) - V_{b,\text{in}}, \tag{17b}$$

and for c port

$$I_{2,c} = I_{4,c} = -I_{1,c} = -I_{3,c}$$

$$= \frac{\sqrt{2}V_{c,\text{in}}}{Z_c} - \frac{\phi_0}{2Z_c}(\dot{\varphi}_2 + \dot{\varphi}_4 - \dot{\varphi}_1 - \dot{\varphi}_3) \tag{18a}$$

$$V_{c,\text{out}} = \frac{\sqrt{2}\phi_0}{2}(\dot{\varphi}_2 + \dot{\varphi}_4 - \dot{\varphi}_1 - \dot{\varphi}_3) - V_{c,\text{in}}. \tag{18b}$$

The extra factor $\sqrt{2}$ that appears for the c port is due to the microwave power being split $50:50$ between the two transmission lines that drive all four nodes simultaneously.

When constructing the EOM with input-output ports, we should consider the current contribution from all the input-output ports together. For example, the net current injected through node 1 should have contributions from the drive applied to both ports for modes a and c, i.e., $I_{1,\text{net}} = I_{1,a} + I_{1,c}$.

B. Full nonlinear equations of motion for the Josephson parametric amplifier

In this subsection, we combine the circuit model for JPA with the input-output relations to construct the full nonlinear EOMs of the JPA. We will take node 1 as an illustrative example and then give the full set of EOMs for the circuit. Note that the left-hand side of the EOM for the closed circuit model of the JRM in Eq. (7) is equivalent to the current relation at node 1, except for a constant factor ϕ_0. To construct the EOM for the open circuit with all the driving ports, we should take the net current injected into node 1 to replace the right-hand side of the Eq. (7). Applying this procedure to all nodes, we obtain the EOMs

$$\ddot{\varphi}_1 + \frac{(3\varphi_1 - \varphi_2 - \varphi_3 - \varphi_4)}{8C_aL_{\text{in}}} + \frac{1}{2C_aL_J}\left[\sin\left(\varphi_1 - \varphi_2 + \frac{\varphi_{\text{ext}}}{4}\right) - \sin\left(\varphi_4 - \varphi_1 + \frac{\varphi_{\text{ext}}}{4}\right)\right] = \frac{1}{2C_a\phi_0}(I_{1,a} + I_{1,c}), \tag{19a}$$

$$\ddot{\varphi}_2 + \frac{(3\varphi_2 - \varphi_1 - \varphi_3 - \varphi_4)}{8C_bL_{\text{in}}} + \frac{1}{2C_bL_J}\left[\sin\left(\varphi_2 - \varphi_3 + \frac{\varphi_{\text{ext}}}{4}\right) - \sin\left(\varphi_1 - \varphi_2 + \frac{\varphi_{\text{ext}}}{4}\right)\right] = \frac{1}{2C_b\phi_0}(I_{2,b} + I_{2,c}), \tag{19b}$$

$$\ddot{\varphi}_3 + \frac{(3\varphi_3 - \varphi_1 - \varphi_2 - \varphi_4)}{8C_aL_{\text{in}}} + \frac{1}{2C_aL_J}\left[\sin\left(\varphi_3 - \varphi_4 + \frac{\varphi_{\text{ext}}}{4}\right) - \sin\left(\varphi_2 - \varphi_3 + \frac{\varphi_{\text{ext}}}{4}\right)\right] = \frac{1}{2C_a\phi_0}(I_{3,a} + I_{3,c}), \tag{19c}$$

$$\ddot{\varphi}_4 + \frac{(3\varphi_4 - \varphi_1 - \varphi_2 - \varphi_3)}{8C_bL_{\text{in}}} + \frac{1}{2C_bL_J}\left[\sin\left(\varphi_4 - \varphi_1 + \frac{\varphi_{\text{ext}}}{4}\right) - \sin\left(\varphi_3 - \varphi_4 + \frac{\varphi_{\text{ext}}}{4}\right)\right] = \frac{1}{2C_b\phi_0}(I_{4,b} + I_{4,c}). \tag{19d}$$

where the net currents injected from each of the ports to the corresponding nodes are given in Eqs. (14), (17), and (18). Using the transformation of Eq. (8), we obtain the EOMs using the normal modes

$$\ddot{\varphi}_a + \gamma_a\dot{\varphi}_a + \frac{\varphi_a}{2C_aL_{\text{in}}} + \frac{2}{C_aL_J}\left[\sin\left(\frac{\varphi_a}{2}\right)\cos\left(\frac{\varphi_b}{2}\right)\cos(\varphi_c)\cos\left(\frac{\varphi_{\text{ext}}}{4}\right) - \cos\left(\frac{\varphi_a}{2}\right)\sin\left(\frac{\varphi_b}{2}\right)\sin(\varphi_c)\sin\left(\frac{\varphi_{\text{ext}}}{4}\right)\right]$$

$$= 2\gamma_a\partial_t\varphi_{a,\text{in}}(t), \tag{20a}$$

$$\ddot{\varphi}_b + \gamma_b\dot{\varphi}_b + \frac{\varphi_b}{2C_bL_{\text{in}}} + \frac{2}{C_bL_J}\left[\cos\left(\frac{\varphi_a}{2}\right)\sin\left(\frac{\varphi_b}{2}\right)\cos(\varphi_c)\cos\left(\frac{\varphi_{\text{ext}}}{4}\right) - \sin\left(\frac{\varphi_a}{2}\right)\cos\left(\frac{\varphi_b}{2}\right)\sin(\varphi_c)\sin\left(\frac{\varphi_{\text{ext}}}{4}\right)\right]$$

$$= 2\gamma_b\partial_t\varphi_{b,\text{in}}(t), \tag{20b}$$

$$\ddot{\varphi}_c + \gamma_c\dot{\varphi}_c + \frac{\varphi_c}{C_cL_{\text{in}}} + \frac{4}{C_cL_J}\left[\cos\left(\frac{\varphi_a}{2}\right)\cos\left(\frac{\varphi_b}{2}\right)\sin(\varphi_c)\cos\left(\frac{\varphi_{\text{ext}}}{4}\right) - \sin\left(\frac{\varphi_a}{2}\right)\sin\left(\frac{\varphi_b}{2}\right)\cos(\varphi_c)\sin\left(\frac{\varphi_{\text{ext}}}{4}\right)\right]$$

$$= \sqrt{2}\gamma_c\partial_t\varphi_{c,\text{in}}(t), \tag{20c}$$

where we define the effective capacitance for the c mode as $C_c = \frac{4C_aC_b}{C_a+C_b}$. The mode decay rates γ_a, γ_b, and γ_c are given by $\gamma_a = (C_aZ_a)^{-1}$, $\gamma_b = (C_bZ_b)^{-1}$, and $\gamma_c = \frac{C_a+C_b}{2C_aC_bZ_c}$. We convert the input-output relations of Eqs. (15), (17b), and (18b) into input-output relations for flux

$$\varphi_{a,\text{out}} = \varphi_a - \varphi_{a,\text{in}}, \tag{21a}$$

$$\varphi_{b,\text{out}} = \varphi_b - \varphi_{b,\text{in}}, \tag{21b}$$

$$\varphi_{c,\text{out}} = \sqrt{2}\varphi_c - \varphi_{c,\text{in}}. \tag{21c}$$

The response of the JPA can be fully described using Eqs. (20) and (21).

Finally, we point out that it is useful to use the normal modes of the JRM as the coordinates for writing the EOMs as it makes the analysis of the effects of the various orders of nonlinear coupling easier to understand. On the other hand, using the node fluxes as coordinates is useful as they are more naturally connected to Kirchhoff's law, especially when we want to include experimental imperfections.

IV. SATURATION POWER OF A JOSEPHSON PARAMETRIC AMPLIFIER (WITH PARTICIPATION RATIO $p = 1$)

In this section, we first obtain the saturation power of the JPA as described by the exact nonlinear EOMs discussed in Subsec. III B. Next, we analyze how higher order nonlinear couplings affect the dynamics of the JPA with the goal of understanding which couplings control the saturation power of the parametric amplifier, to give us guidance on how to improve the saturation power.

We begin with Subsec. IV A, in which we summarize our main results concerning the dependence of the saturation power on the parameter

$$\beta = L_J/L_{\text{in}}. \tag{22}$$

Specifically, we compare numerical solution of the full nonlinear model with numerical solutions of truncated models as well as perturbation theory results. We show that for small β the limitation on saturation power comes from dynamically generated Kerr-like terms, while for large β saturation power is limited by fifth-order nonlinearities of the JRM. The details of the analytical calculations are provided in the following subsections.

In Subsec. IV B, we remind ourselves of the exact analytical solution for the ideal third-order amplifier in which the signal is so weak that it does not perturb the pump (i.e., the stiff-pump case). Next, in Subsec. IV C we consider the case of a third-order amplifier with input signal sufficiently strong such that it can affect the pump (i.e., the soft pump case). In this subsection, we construct a classical perturbation expansion (in which the stiff pump solution corresponds to the zeroth-order solution and the first-order correction) and find that it leads to the generation of an effective cross-Kerr term and a pair of two-photon loss terms, one of which could be thought of as an imaginary cross-Kerr term. In Subsec. IV D, we compare the effects of the dynamically generated terms to intrinsic Kerr terms. We analyze fifth- and higher order couplings in Subsec. IV E.

A note about notation: Throughout this section, we refer to the a mode as the signal mode, b mode as the idler mode, and c mode as the pump mode with intrinsic frequencies ω_a, ω_b, and ω_c. To simplify the discussion of the perturbative expansion, we only consider the case in which we assume that (1) the parametric amplifier is on resonance, i.e., $\delta = \omega_S - \omega_a = 0$ (where ω_S is the frequency of the signal tone) and $\varepsilon_p = \omega_P - (\omega_a + \omega_b) = 0$ (where ω_P is the pump tone frequency), so that $\omega_S = \omega_a$, $\omega_I = \omega_b$ and $\omega_P = \omega_a + \omega_b$, (2) the magnetic flux bias is set to the Kerr nulling point, i.e., $\varphi_{\text{ext}} = 2\pi$, (3) an input tone is only sent to the signal mode and there is no input to the idler mode.

A. Main result: Saturation power as a function of β

In this subsection, we will compare the exact numerical solution of the full nonlinear EOMs of the JPA to various approximate solutions in order to identify the effects that limit saturation power.

For concreteness, we fix the following parameters: The magnetic field bias is fixed at $\varphi_{\text{ext}} = 2\pi$, the mode frequencies are fixed at $\omega_a/(2\pi) = 7.5$ GHz and $\omega_b/(2\pi) = 5.0$ GHz ($\omega_c/(2\pi) = 6.37$ GHz is fixed by the JPA circuit), the decay rates of the modes are fixed at $\gamma_a/(2\pi) = \gamma_b/(2\pi) = \gamma_c/(2\pi) = 0.1$ GHz, and the critical current of the Josephson junctions is fixed at $i_c = 1\ \mu$A. Throughout, we will set the amplitude of the pump to achieve 20-dB reflection gain (at small signal powers). This leaves us with one independent parameter: the JRM inductance ratio β.

We shall now analyze saturation of the amplifier as a function of β. We find it convenient to use saturation input signal flux $|\varphi_{a,\text{in}}(\omega_a)|$ as opposed to $P_{\pm 1\text{dB}}$ because the former saturates to a constant value at high β while the latter grows linearly at high β. We note that the two quantities are related by the formula

$$P_{\pm 1\text{dB}} = \frac{\phi_0^2}{2Z_a}\left|\partial_t^2\varphi_{a,\text{in}}(t)\right|^2 = \frac{1}{2}C_a\phi_0^2\gamma_a\omega_a^2|\varphi_{a,\text{in}}(\omega_a)|^2. \tag{23}$$

At the nulling point, the EOMs do not explicitly depend on the Josephson junction critical current i_c. Therefore, the dynamics of the circuit in terms of the dimensionless fluxes φ_a, φ_b, and φ_c are invariant if we fix ω_a, ω_b, γ_a, γ_b, γ_c, and β. However, i_c is needed to connect the dimensionless fluxes to dimensional variables. Specifically, the connection requires the mode capacitance; see Eq. (23). At the nulling point, the mode capacitance is set by the mode frequency and L_{in} [e.g., $C_a = 1/(\omega_a^2 L_{\text{in}})$] and L_{in} is set by i_c; see Eq. (22). In the following, we will analyze saturation power in terms of dimensionless fluxes.

In Fig. 3, we plot the saturation flux as a function of β obtained using the full nonlinear EOMs as well as various truncated EOMs and perturbation theory. In Fig. 3(a), we use the conventional criteria that saturation occurs when the gain change by ± 1 dB, while in Fig. 3(b) we use the tighter condition that gain changes by ± 0.1 dB. We observe that the saturation flux has two different regimes. At small β the saturation flux grows linearly with β, while at high β it saturates to a constant.

To understand the limiting mechanisms in both β regimes, we compare the saturation flux $\varphi_{a,\text{in}}$ obtained from the
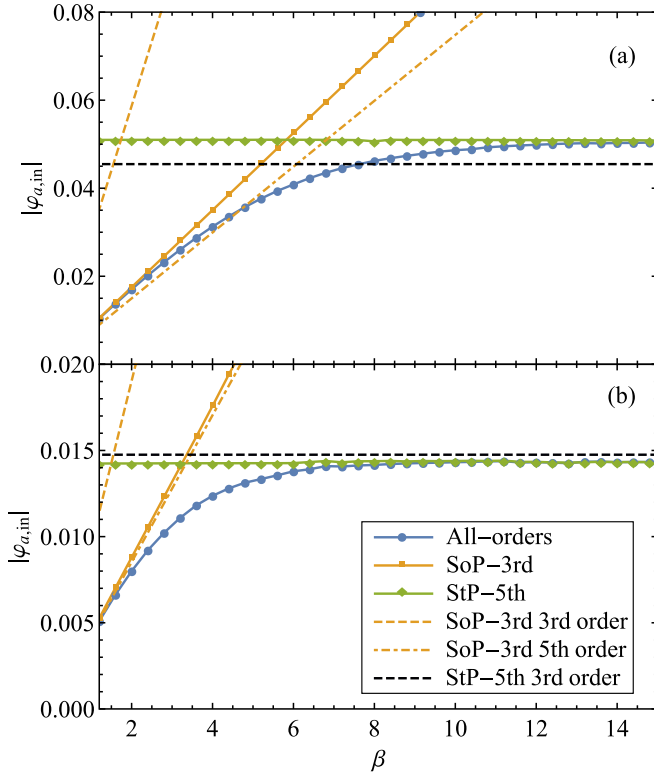
FIG. 3. We plot the saturation flux $|\varphi_{a,\text{in}}|$ of the JPA as we change JRM inductance ratio $\beta = L_J/L_{\text{in}}$. The amplifier saturates to 19 and 19.9 dB in panels (a) and (b) respectively. The saturation flux from numerical integration of full nonlinear EOMs, SoP third-order, and StP fifth-order nonlinear models of JPA are plotted as blue, orange, and dark green solid lines in both subplots. The saturation fluxes are also obtained by the perturbation analysis for the SoP third-order and StP fifth-order nonlinear models. We plot the third- and fifth-order perturbation results as dashed lines and dash-dotted lines. In panel (a), the perturbation saturation fluxes do not agree well with the numerical ones. This is because the saturation fluxes are already out of the radius of convergence of the perturbation series. In panel (b), they have a good agreement. Parameters chosen are $\varphi_{\text{ext}} = 2\pi$, the mode frequencies $\omega_a/(2\pi) = 7.5$ GHz, $\omega_b/(2\pi) = 5.0$ GHz, and mode decay rates $\gamma/(2\pi) = 100$ MHz for all three modes. The critical current is set to $i_c = 1$ μA. We tune the inner shunted inductance L_{in} to tune β.

numerical integration of full nonlinear EOMs with the various truncated EOMs. We mainly focus on two nonlinear truncated models: (1) soft-pump third-order truncated model (SoP third), in which the EOMs of the amplifier are obtained by truncating the Josephson energy to third order in mode fluxes; (2) the stiff-pump fifth-order truncated model (StP fifth), in which the Josephson energy is truncated to fifth order in mode fluxes and we ignore the backaction of the signal and idler modes on pump mode dynamics.

We begin by considering the small-β regime. Comparing the saturation flux obtained from the numerical integration of full nonlinear EOMs with the above two truncated EOMs, we see that the saturation flux $\varphi_{a,\text{in}}$ of the full nonlinear EOMs most closely matches the EOMs of SoP third-order model of the amplifier, which indicates the soft-pump condition is the dominating limitation in this regime.

In the soft-pump model, saturation power is limited by the dynamically generated Kerr term. This term shifts the signal and idler modes off resonance as the power in these modes builds up. We describe the details of this process in Subsecs. IV C and IV D. In the small-β regime, the saturation flux of the amplifier increases as we increase β [see Fig. 3(a)]. This is because increasing β effectively decreases the nonlinear coupling strength of the amplifier and therefore decreasing the effective strength of the dynamically generated Kerr term. This conclusion is supported by comparing (see Fig. 3) the exact numerics on the SoP third model (labeled SoP third) with a perturbative analysis of the same model which captures the generated Kerr terms (labeled SoP third fifth order).

In the large-β regime, the saturation flux obtained from full nonlinear model saturates to a constant value (see Fig. 3, "all-order" line). This behavior diverges from the prediction of the SoP third-order nonlinear model ("SoP third" line) but it is consistent with the StP fifth-order nonlinear model ("StP fifth" line), which indicates that the dominating limitation in the large-β regime is the intrinsic fifth-order nonlinearity of the JRM energy. Perturbation theory analysis of the StP fifth-order nonlinear model ("StP fifth third order" and "StP fifth fifth order" lines; see Subsec. IV E) indicates that the saturation flux depends on the ratio of the fifth-order and the third-order nonlinear couplings arising from the Josephson nonlinearity, and is therefore independent of β. As we increase β, the limitation on the saturation power placed by the generated cross-Kerr couplings decreases and hence the mechanism limiting the amplifier's saturation flux changes from generated cross-Kerr couplings to fifth-order nonlinearity of the JRM energy. The β at which the mechanism controlling saturation flux changes is controlled by the decay rates as $\beta \propto \gamma^{-1/2}$. For our choice of parameters, this change of mechanism occurs at $\beta \sim 6$.

B. Ideal parametric amplifier, third-order coupling with stiff pump approximation

In this subsection, we remind ourselves with the solution of ideal parametric amplifier. The ideal parametric amplifier can be exactly solved in frequency domain such that we can also verify the reliability of the numerical solutions.

In an ideal parametric amplifier, the only coupling present is a third-order coupling of the signal, idler, and pump mode that results in parametric amplification. Further, the pump mode strength is considered to be strong compared to the power consumed by the amplification, such that the pump mode dynamics can be treated independently of the signal and idler modes. This approximation is commonly referred to as the "stiff-pump approximation" (StP). The EOMs to describe the parametric amplifier can be derived from the full nonlinear EOMs in Eq. (20) by expanding the nonlinear coupling terms to second order in mode fluxes φ's (second order in EOMs corresponding to third order in Lagrangian). Under the stiff-pump approximation, we can effectively remove the three mode coupling terms in the EOM for the pump mode

$$\ddot{\varphi}_c + \gamma_c\dot{\varphi}_c + \omega_c^2\varphi_c = \sqrt{2}\gamma_c\partial_t\varphi_{c,\text{in}}(t). \tag{24}$$

φ_c obtained from this equation acts as a time-dependent parameter in the EOMs for the a and b modes:

$$\ddot{\varphi}_a + \gamma_a \dot{\varphi}_a + \omega_a^2 \varphi_a - \frac{2\omega_a^2}{\beta}\varphi_b \varphi_c = 2\gamma_a \partial_t \varphi_{a,\text{in}}(t), \quad (25a)$$

$$\ddot{\varphi}_b + \gamma_b \dot{\varphi}_b + \omega_b^2 \varphi_b - \frac{2\omega_b^2}{\beta}\varphi_a \varphi_c = 2\gamma_b \partial_t \varphi_{b,\text{in}}(t). \quad (25b)$$

Assuming the pump tone is $\varphi_{c,\text{in}}(t) = \varphi_{c,\text{in}}e^{-i\omega_P t} + \text{c.c.}$, we find that $\varphi_c(t) = \varphi_c(\omega_P)e^{-i\omega_P t} + \text{c.c.}$, where

$$\varphi_c(\omega_P) = \frac{-i\sqrt{2}\gamma_c \omega_P}{\omega_c^2 - \omega_P^2 - i\gamma_c \omega_P}\varphi_{c,\text{in}}. \quad (26)$$

After substituting the c-mode flux φ_c in Eq. (25), the EOMs for a and b modes become linear and can be solved in the frequency domain. The Fourier components of the a and b modes, under the rotating-wave approximation, are

$$\varphi_a(\omega_a) = \frac{2\tilde{\gamma}_a \tilde{\gamma}_b}{\tilde{\gamma}_a \tilde{\gamma}_b - 4g^2 |\varphi_c(\omega_P)|^2}\varphi_{a,\text{in}}, \quad (27a)$$

$$\varphi_b^*(\omega_b) = \frac{4ig\tilde{\gamma}_a \varphi_c^*(\omega_P)}{\tilde{\gamma}_a \tilde{\gamma}_b - 4g^2 |\varphi_c(\omega_P)|^2}\varphi_{a,\text{in}}, \quad (27b)$$

where we define the dimensionless decay rates $\tilde{\gamma}_j = \gamma_j/\omega_j$ and the dimensionless three-mode coupling strength $g = (1/\beta)\sin(\frac{\varphi_{\text{ext}}}{4}) = 1/\beta$, which is obtained from a series expansion of the dimensionless potential energy

$$\mathcal{E}_{\text{JRM}} \equiv \left[(\phi_0^2/L_{\text{in}})\right]^{-1} E_{\text{JRM}}. \quad (28)$$

Here we assume the input tone is $\varphi_{a,\text{in}} = \varphi_{a,\text{in}}e^{-i\omega_a t} + \text{c.c.}$ and there is no input into idler (b) mode.

The linear response of the ideal parametric amplifier is obtained using scattering matrix formalism. The EOMs of an ideal parametric amplifier can be written in matrix form as $[M][\varphi] = 2[\tilde{\gamma}][\varphi_{\text{in}}]$, where

$$[M] = \begin{pmatrix} \tilde{\gamma}_a & -2ig\varphi_c(\omega_P) \\ 2ig\varphi_c^*(\omega_P) & \tilde{\gamma}_b \end{pmatrix}, \quad (29)$$

$$[\tilde{\gamma}] = \begin{pmatrix} \tilde{\gamma}_a & \\ & \tilde{\gamma}_b \end{pmatrix}. \quad (30)$$

The scattering matrix, which is defined by $[\varphi_{\text{out}}] = [S][\varphi_{\text{in}}]$, is given by $[S] = 2[M^{-1}][\tilde{\gamma}] - I_{2\times 2}$, where we have used the input-output relation $[\varphi] = [\varphi_{\text{in}}] + [\varphi_{\text{out}}]$ and $I_{2\times 2}$ is the 2×2 identity matrix,

$$[S] = \begin{pmatrix} \frac{2\tilde{\gamma}_a \tilde{\gamma}_b}{\tilde{\gamma}_a \tilde{\gamma}_b - 4g^2|\varphi_c(\omega_P)|^2} - 1 & -\frac{4ig\tilde{\gamma}_b \varphi_c(\omega_P)}{\tilde{\gamma}_a \tilde{\gamma}_b - 4g^2|\varphi_c(\omega_P)|^2} \\ \frac{4ig\tilde{\gamma}_a \varphi_c^*(\omega_P)}{\tilde{\gamma}_a \tilde{\gamma}_b - 4g^2|\varphi_c(\omega_P)|^2} & \frac{2\tilde{\gamma}_a \tilde{\gamma}_b}{\tilde{\gamma}_a \tilde{\gamma}_b - 4g^2|\varphi_c(\omega_P)|^2} - 1 \end{pmatrix}. \quad (31)$$

The reflection gain of the signal mode (in units of power) is defined as $G_0 = |[S]_{11}|^2$. To get large gain ($G_0 \gg 1$), the pump mode strength should be tuned to

$$2g|\varphi_c(\omega_P)| \sim \sqrt{\tilde{\gamma}_a \tilde{\gamma}_b}. \quad (32)$$

Alternatively, we can obtain the response of the JPA using time-domain numerical integration. First, we solve for the mode variables inside the JPA circuit with specific signal and pump inputs. Next, we use the input-output relation to find the output signal and then we obtain the reflection gain of the amplifier. Specifically, to solve the dynamics of the parametric
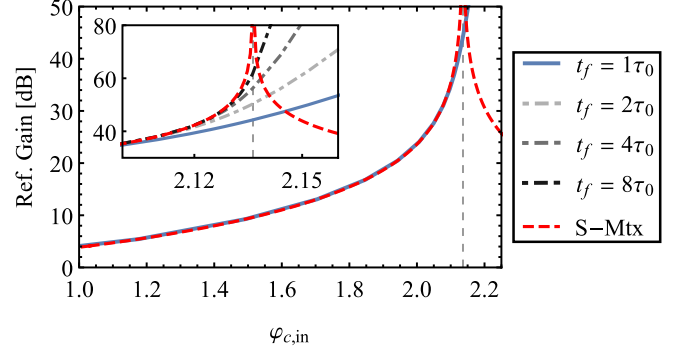

FIG. 4. The reflection gain of an ideal parametric amplifier calculated by both scattering matrix (blue curve) and time-domain numerical evolution (red dashed line). The response of the ideal amplifier can be faithfully simulated by the time-domain numerical method with a reasonable reflection gain. The black dashed line shows the bias point beyond which the amplifier is unstable. Our time-domain numerical solution start to deviated form the scattering matrix calculation at ≈ 2.1. This is because the numerical accuracy of the time-domain solver. In the insert, we increase the final time t_f of the time solver. We notice a better and better convergence to the analytical solution (red dashed line). This is caused by a numerical instability that occurs near the divergence point of the amplifier, Eq. (32). Parameters chosen: $\varphi_{\text{ext}} = 2\pi$, $\omega_a/(2\pi) = 7.5$ GHz, $\omega_b/(2\pi) = 5.0$ GHz, $\gamma_a = \gamma_b = \gamma_c = 2\pi \times 0.01$ GHz, and $i_c = 1.0$ μA. Time constant $\tau_0 = 4000 f_a^{-1}$, where f_a is the signal mode frequency.

amplifier, we set the input signal as $\varphi_{a,\text{in}}(t) = \bar{\varphi}_{a,\text{in}}\cos(\omega_S t)$ and $\varphi_{b,\text{in}} = 0$, and numerically integrate the EOMs [Eq. (25)]. Here we note that $\bar{\varphi}_{a,\text{in}} = 2\varphi_{a,\text{in}}$, which is defined in Eq. (27). In Fig. 4, we show the comparison of the reflection gain obtained using numerical integration (red dashed line) and the scattering matrix solution (blue solid line). The two solutions start out identical. However, as we increase the pump mode strength $\varphi_{c,\text{in}}$, we notice that as the reflection gain starts diverging ($G_0 \sim 35$ dB; see the insert of Fig. 4) from the analytical solution. This is because the numerical solver needs a longer time window to establish the steady-state solution of the nonlinear EOMs as we move toward the unstable point (vertical dashed line). To optimize the run time, here and later in the paper, we choose the time window for our solver so that the numerical solution saturates for amplification of ≈ 20 dB.

In the unstable regime, the reflection flux on the signal mode diverges exponentially with time, as the amplifier will never run out of power under the StP approximation. Therefore, in this regime the time-domain solver gives a large unphysical reflection gain (as we cut it off at some large but finite time).

C. JPA with third-order coupling, relaxing the stiff-pump approximation

As we increase the input signal strength, the power supplied to the pump mode will eventually be comparable to the power consumed by amplification, where the amplifier will significantly deviate from the ideal parametric amplifier. In this subsection, we reinstate the action of the signal and idler modes on the pump mode. Since the pump mode strength is
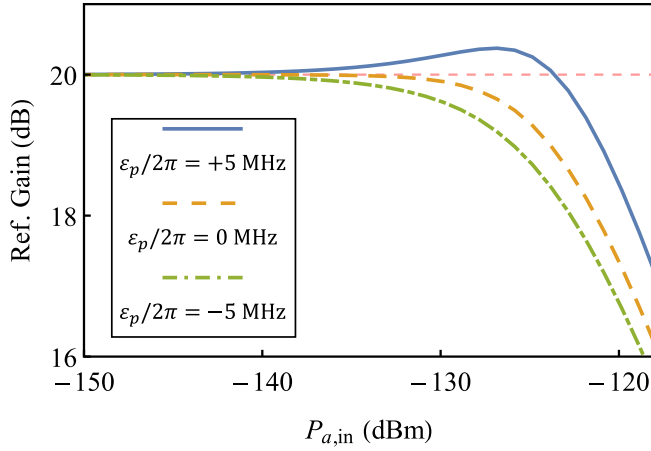
FIG. 5. We consider the soft-pump condition with third-order coupling strength and calculate the reflection gain of the amplifier. We slightly detune the pump drive frequency from the sum frequency of the signal and idler mode frequency. When the pump frequency detuning ε_p is negative (green dash-dotted line), the reflection gain is further suppressed compared with on-resonance drive (orange dashed line). However, when the pump frequency detuning is positive (blue line), the "shark fin" feature reappears, which was understood as the consequence of the existence of Kerr nonlinearity in the amplifier system.

affected by the signal and idler mode strengths, we refer to it as the "soft-pump" (SoP) condition.

The EOMs for the soft-pump third-order model of the JPA can be obtained by expanding the full nonlinear EOMs [Eq. (20)] and truncating all three EOMs to second order in mode fluxes. That is, we use Eq. (25) to describe a and b modes and modify Eq. (24) for the c mode as

$$\ddot{\varphi}_c + \gamma_c \dot{\varphi}_c + \omega_c^2 \varphi_c - \frac{\omega_c^2}{\beta} \varphi_a \varphi_b = \sqrt{2} \gamma_c \partial_t \varphi_{c,\text{in}}(t). \quad (33)$$

Unlike the StP approximation, the c mode flux φ_c can no longer be treated as a time-dependent parameter unaffected by a and b modes. While we can no longer obtain an exact analytical solution to these EOMs, we use perturbation theory as well as time-domain numerical integration to seek the dynamics of the amplifier.

In Fig. 5, we plot the reflection gain obtained by numerical integration. The reflection gain of the amplifier is no longer independent of the input signal power; instead we see that the reflection gain deviates from 20 dB as we increase the signal mode power. Moreover, as we change the detuning of the pump mode relative to the sum frequency of the signal and idler mode, the deviation of the reflection gain changes from negative to positive. While a deviation toward smaller gain (which occurs at negative or zero detuning) is consistent with the pump saturation scenario, a deviation toward higher gain (which occurs at positive detuning) is not. The "shark fin" feature we observe here, in which the gain first deviates up and then down, has been previously attributed to intrinsic Kerr couplings [24]. The fact that the "shark fin" reappears without an intrinsic Kerr term gives us a hint that SoP third-order couplings can generate an effective Kerr nonlinearity.

To fully understand the effect of the SoP condition, we use classical perturbation theory to analyze the dynamics of the circuit. Below, we explain the essential steps of the perturbation analysis. Then, we focus on the SoP third-order truncated model and compute the parametric dependence of the saturation flux of the amplifier.

1. Classical perturbation theory for the Josephson parametric amplifier

The small parameter in our perturbative expansion is the input fluxes to the signal and idler modes, $\varphi_{a,\text{in}}$ and $\varphi_{b,\text{in}}$. We can expand the mode fluxes in a series as

$$\varphi_j(t) = \varphi_j^{(0)}(t) + \varphi_j^{(1)}(t) + \varphi_j^{(2)}(t)... \quad (34)$$

for $j = a, b, c$. The EOM of the signal mode flux φ_a after series expansion is

$$\left(\partial_t^2 + \gamma_a \partial_t + \omega_a^2\right)\left[\varphi_a^{(1)}(t) + \varphi_a^{(2)}(t) + \cdots\right]$$
$$- \frac{2\omega_a^2}{\beta}\left[\varphi_b^{(1)}(t) + \varphi_b^{(2)}(t) + \cdots\right]\left[\varphi_c^{(0)}(t) + \varphi_c^{(1)}(t) + \cdots\right]$$
$$= 2\gamma_a \partial_t \varphi_{a,\text{in}}(t). \quad (35)$$

The idler and pump mode EOMs are similar.

In the absence of inputs to the signal and idler modes, we obtain the zeroth-order solution of the EOMs. Since the amplifier should be stable, there should be no output in the signal and idler modes when there is no input, i.e., $\varphi_a^{(0)} = \varphi_b^{(0)} = 0$. Therefore, the only nonzero zeroth-order solution is for the pump mode, which is given by

$$\ddot{\varphi}_c^{(0)} + \gamma_c \dot{\varphi}_c^{(0)} + \omega_c^2 \varphi_c^{(0)} = \sqrt{2} \gamma_c \partial_t \varphi_{c,\text{in}}(t). \quad (36)$$

This equation matches the StP c mode EOM [see Eq. (24)]; the zeroth-order solution for φ_c is given in Eq. (26). We can then solve the higher corrections to signal, idler, and pump mode fluxes by matching the terms in the EOMs order by order. For example, the equations for first-order corrections $\varphi_a^{(1)}$ and $\varphi_b^{(1)}$ are identical to the ideal parametric amplifier, and hence they are given by the StP solution Eq. (27), while the first-order correction to the pump mode flux is $\varphi_c^{(1)} = 0$.

As the first-order correction to the pump mode is zero, there are no second-order corrections to the signal and idler mode fluxes. The second-order correction to the pump mode has two frequency components, $\Sigma = \omega_S + \omega_I$ and $\Delta = \omega_S - \omega_I$, with Fourier components

$$\varphi_c^{(2)}(\Sigma) = f_\Sigma \frac{1}{\beta} \varphi_a^{(1)}(\omega_S)\varphi_b^{(1)}(\omega_I), \quad (37a)$$

$$\varphi_c^{(2)}(\Delta) = f_\Delta \frac{1}{\beta} \varphi_a^{(1)}(\omega_S)\varphi_b^{(1)*}(\omega_I), \quad (37b)$$

where the two dimensionless parameters f_Σ and f_Δ are defined as

$$f_\Sigma = \frac{\omega_c^2}{\omega_c^2 - \Sigma^2 - i\gamma_c \Sigma}, \quad (38a)$$

$$f_\Delta = \frac{\omega_c^2}{\omega_c^2 - \Delta^2 - i\gamma_c \Delta}. \quad (38b)$$

Both of these two frequency components contribute to the third-order correction to the signal and idler mode flux with frequency ω_S and ω_I.

To obtain the third-order corrections to the signal and idler mode fluxes, we define an effective drive vector that is composed of all the contributions from lower orders, utilizing Eq. (37) to express $\varphi_c^{(2)}$ in terms of $\varphi_a^{(1)}$ and $\varphi_b^{(1)}$

$$\left[\varphi_d^{(3)}\right] = \begin{pmatrix} 2g^2(f_\Delta + f_\Sigma)\varphi_a^{(1)}\left|\varphi_b^{(1)}\right|^2 \\ 2g^2(f_\Delta + f_\Sigma^*)\varphi_b^{(1)*}\left|\varphi_a^{(1)}\right|^2 \end{pmatrix}. \qquad (39)$$

The third-order correction to the signal and idler mode is given by $[\varphi^{(3)}] = [M^{-1}][i][\varphi_d^{(3)}]$, where $[M]$ is the same matrix as in the discussion of the ideal parametric amplifier Eq. (29), and $[i] = \mathrm{diag}\{i, -i\}$ is a diagonal 2×2 matrix. The signal mode third-order correction is

$$\varphi_a^{(3)} = \left(\frac{1}{\beta}\right)^2 \left\{ 2i[M^{-1}]_{11}(f_\Sigma + f_\Delta)\varphi_a^{(1)}\left|\varphi_b^{(1)}\right|^2 \right. $$
$$\left. - 2i[M^{-1}]_{21}(f_\Sigma^* + f_\Delta)\varphi_b^{(1)*}\left|\varphi_a^{(1)}\right|^2 \right\}. \qquad (40)$$

Using this expression, we obtain the corrections to the reflection gain up to second order $G^{(2)} = |\varphi_a^{(1)}(\omega_S) + \varphi_a^{(3)}(\omega_S) - \varphi_{a,\mathrm{in}}|^2/|\varphi_{a,\mathrm{in}}|^2$. Similarly, we can solve the perturbation theory order by order until the desired order.

Here we want to stress that we only focus on the main frequency components of signal and idler modes, i.e., $\varphi_a(\omega_a)$ and $\varphi_b(\omega_b)$ and ignore the higher order harmonics. This assumption is also applied when we consider the higher than third-order nonlinear couplings in the JPA truncated EOMs, e.g., in StP-Kerr nonlinear truncated model (discussed in Subsec. IV D) and StP fifth-order truncated model (discussed in Subsec. IV E).

Further, we point out that the above discussion is easily generalized to the case when $\omega_S \neq \omega_a$, $\omega_I \neq \omega_b$, and (or) $\varphi_{\mathrm{ext}} \neq 2\pi$.

Next, we consider the question of how the perturbation on the reflection gain can be used to compute the saturation power of the amplifier. The saturation power is defined as the input power at which the amplifier's reflection gain changes by 1 dB. At the limit $\varphi_{a,\mathrm{in}} \to 0$, the reflection gain of the amplifier is noted as G_0, which is given by $G_0 = |\varphi_a^{(1)} - \varphi_{a,\mathrm{in}}|^2/|\varphi_{a,\mathrm{in}}|^2$.

As we increase the input signal strength $\varphi_{a,\mathrm{in}}$ to reach 1 dB suppression of the reflection gain, the corrected gain (in power unit) should satisfy

$$G = \frac{\left|\varphi_a^{(1)} + \varphi_a^{(c)} - \varphi_{a,\mathrm{in}}\right|^2}{|\varphi_{a,\mathrm{in}}|^2} = 10^{-0.1}G_0, \qquad (41)$$

where $\varphi_a^{(c)}$ is the higher order corrections to the signal mode flux in perturbation theory. In the high gain limit ($G_0 \gg 1$), we can estimate the criteria by

$$\left|\varphi_a^{(c)}\right|/\left|\varphi_a^{(1)}\right| = \epsilon \equiv 10^{-0.05} - 1. \qquad (42)$$

Note ϵ depends on the definition of the threshold for the gain change at the amplifier saturation.

2. Perturbative analysis on SoP third-order EOM

We apply the above perturbation analysis to SoP third-order truncated model to understand the mechanism of amplifier saturation in this model. Before we proceed to calculate the corrections to the reflection gain, we estimate the matrix elements in the inverse of the parametric matrix $[M]$ [see Eq. (29)] in high gain limit, i.e.,

$$G_A \equiv \sqrt{G_0} = 2\tilde{\gamma}_a[M^{-1}]_{11} - 1$$
$$= \frac{2\tilde{\gamma}_a\tilde{\gamma}_b}{\tilde{\gamma}_a\tilde{\gamma}_b - 4g^2|\varphi_c(\omega_P)|^2} - 1 \gg 1. \qquad (43)$$

Therefore, we can approximate $2\tilde{\gamma}_a[M^{-1}]_{11} \sim G_A$ and hence $\varphi_a^{(1)}(\omega_a) \sim G_A\varphi_{a,\mathrm{in}}$. The matrix element $[M^{-1}]_{21}$ can be approximated by $-iG_A/(2\sqrt{\tilde{\gamma}_a\tilde{\gamma}_b})$, which can be seen from the relation $[M^{-1}]_{21} = -i2g\varphi_c^{(0)*}([M^{-1}]_{11})/\tilde{\gamma}_b$ and $\sqrt{\tilde{\gamma}_a\tilde{\gamma}_b} \sim 2g|\varphi_c^{(0)}|$.

The third-order correction to signal mode strength is given by the Eq. (40), which becomes

$$\varphi_a^{(3)}(\omega_b) \sim 2\frac{g^2}{\tilde{\gamma}_a}G_A^4\,\mathrm{Im}(f_\Sigma)\varphi_{a,\mathrm{in}}^3 \qquad (44)$$

in the high-gain approximation.

To calculate the saturation flux, we let $\varphi_a^{(3)} \sim \epsilon\varphi_a^{(1)}$ and solve for $\varphi_{a,\mathrm{in}}$, where ϵ is given in Eq. (42). The saturation flux given by third-order perturbation is

$$\varphi_{a,\mathrm{in},\pm1\,\mathrm{dB}} \sim G_0^{-3/4}\sqrt{\epsilon}\frac{\sqrt{\tilde{\gamma}_b}}{g}\mathrm{Im}(f_\Sigma)^{-1/2}, \qquad (45)$$

where G_0 is the small-signal reflection gain of the amplifier. The saturation flux given by third-order perturbation theory of SoP third-order nonlinear model is plotted as orange (light gray) dashed line in Fig. 3(a) [41]. We notice that the saturation flux predicted by third-order perturbation theory does not agree well with the numerical simulation ("SoP third" line). The disagreement also occurs when we tighten the criteria for amplifier saturation to 0.1 dB [see Fig. 3(b) "SoP third third-order" line].

To explain the disagreement between the perturbation theory and the numerical integration method, we correct the signal mode flux to the next nonzero order, which is at fifth order in $\varphi_{a,\mathrm{in}}$. To solve the fifth-order correction of signal and idler mode fluxes, we follow the same strategy as demonstrated above. The only nonzero fourth-order correction is $\varphi_c^{(4)}$, with two frequency components, $\varphi_c^{(4)}(\Sigma)$ and $\varphi_c^{(4)}(\Delta)$. The fifth-order correction to the signal mode strength $\varphi_a^{(5)}$ is

$$\varphi_a^{(5)} \sim \frac{g^4}{\tilde{\gamma}^2}G_0^{5/2}\mathrm{Re}[f_\Sigma + f_\Delta]^2\varphi_{a,\mathrm{in}}^5, \qquad (46)$$

where we use the fact that imaginary parts of f_Δ and f_Σ are much smaller than their real parts and hence we ignore the contribution from their imaginary parts. The saturation flux can be estimated by $|\varphi_a^{(5)}| \sim \epsilon|\varphi_a^{(1)}|$ as

$$\varphi_{a,\mathrm{in},\pm1\,\mathrm{dB}} \sim G_0^{-5/8}\frac{\sqrt{\tilde{\gamma}_b}}{g}\left[\frac{\epsilon}{2}\mathrm{Re}(f_\Sigma + f_\Delta)^{-1}\right]^{1/4}. \qquad (47)$$

Compared with the saturation flux given by third-order perturbation, the fifth-order correction is more significant as f_Δ and f_Σ are almost real. However, in third-order perturbation theory, the contribution of real parts of f_Δ and f_Σ

is canceled, but they will appear in next order perturbation, which dominates the saturation.

The saturation flux correction until fifth-order perturbation is obtained by directively solving Eq. (41) for $\varphi_{a,\text{in}}$, where the corrections of signal mode strength $\varphi_a^{(c)} = \varphi_a^{(3)} + \varphi_a^{(5)}$. The saturation flux corrected up to fifth order ["SoP third fifth-order" line in Figs. 3(a) and 3(b)] have better agreement with the numerical solution.

However, in both third- and fifth-order perturbation analysis, the saturation flux with 1-dB gain change does not agree well with the numerical solution [see Fig. 3(a)]. This is because the saturation flux for ± 1 dB is beyond the radius of convergence of the perturbation series. In order to validate the perturbation analysis, we tighten the criteria for amplifier saturation to change of the amplifier gain by ± 0.1 dB, which makes the signal flux stay in the radius of convergence. In Fig. 3(b), the saturation flux corrected to fifth order ("SoP third fifth-order" line) has a much better agreement with the numerical methods ["SoP third" line in Fig. 3(b)].

We notice that the saturation flux is inversely proportional to $g = 1/\beta$, and hence we expect that it can be increased by decreasing the three-mode coupling strength (increasing β). At the same time, the pump strength must be increased in order to reach G_0. This procedure, in effect, makes the pump stiffer.

D. Intrinsic and generated Kerr couplings

In this subsection, we comment on the generation of effective Kerr terms and compare it with the intrinsic cross-Kerr couplings in the Lagrangian. In the perturbation analysis, if we expand the pump mode strength to second order, the effective EOMs of the signal and idler modes contains a cross-Kerr coupling term, in the form of $\varphi_a|\varphi_b|^2$ for the signal mode and $|\varphi_a|^2\varphi_b$ for the idler mode [see, e.g., Eq. (40)]. We will show that these generated Kerr terms limit the saturation power (at least for small β).

To construct an understanding of this mechanism, we use perturbation theory to analyze the StP amplifier with an intrinsic cross Kerr k_{ab} and compare it with the SoP third-order nonlinear amplifier. As we discussed in Subsec. IV B, in the

stiff pump approximation, we treat the pump mode flux, φ_c, as a time-dependent parameter that is independent of the signal and idler modes. The EOMs for the signal and idler modes can be obtained by adding the terms $4k_{ab}\varphi_a\varphi_b^2$ and $4k_{ab}\varphi_a^2\varphi_b$ to the left-hand-side of Eqs. (25a) and (25b), respectively.

In perturbation analysis, following the discussion in the previous subsection, we expand the signal and idler mode fluxes in the order of $\varphi_{a,\text{in}}$ and $\varphi_{b,\text{in}}$. We further assume that the amplifier is stable; i.e., there is no output from the amplifier if there is no input, which gives the zeroth-order solution of signal and idler modes as $\varphi_a^{(0)} = \varphi_b^{(0)} = 0$. The first-order solution of signal and idler mode fluxes repeats the solution of ideal parametric amplifier [Eq. (27)] and the next nonzero correction appears at third order. The corresponding drive term is

$$\left[\varphi_d^{(3)}\right] = \begin{pmatrix} 8k_{ab}\varphi_a^{(1)}(\omega_S)\left|\varphi_b^{(1)}(\omega_I)\right|^2 \\ 8k_{ab}\varphi_b^{(1)*}(\omega_I)\left|\varphi_a^{(1)}(\omega_S)\right|^2 \end{pmatrix}. \quad (48)$$

Comparing with Eq. (39), we see that the soft-pump condition gives an effective signal-idler Kerr coupling strength

$$k_{ab}^{\text{eff}} = \tfrac{1}{4}g^2[f_\Delta + \text{Re}(f_\Sigma)]. \quad (49)$$

We note that this effective Kerr coupling is complex as f_Δ is complex. We also observe that there is an additional term in Eq. (39) that we label $q_{ab}^{\text{eff}} = (1/4)g^2\text{Im}(f_\Sigma)$, which cannot be mapped onto a Kerr coupling (as the signal and idler parts have opposite sign).

Further, as the intrinsic cross-Kerr coupling k_{ab} is real, the third-order correction to the signal mode in StP cross-Kerr amplifier model is zero. If we proceed to next-nonzero-order correction to the signal and idler mode, and compare the drive term with the one from StP third-order truncated model in same perturbation order, we identify the same effective Kerr coupling strength as Eq. (49).

To check the correspondence and understand to what degree the saturation power of SoP third-order amplifier is limited by the generated effective Kerr coupling, we manually add an intrinsic cross-Kerr coupling, $k_{ab}\varphi_a^2\varphi_b^2$, in the SoP third-order truncated Lagrangian, and observe the saturation power of the amplifier as we tune k_{ab} [see Figs. 6(a) and 6(b),
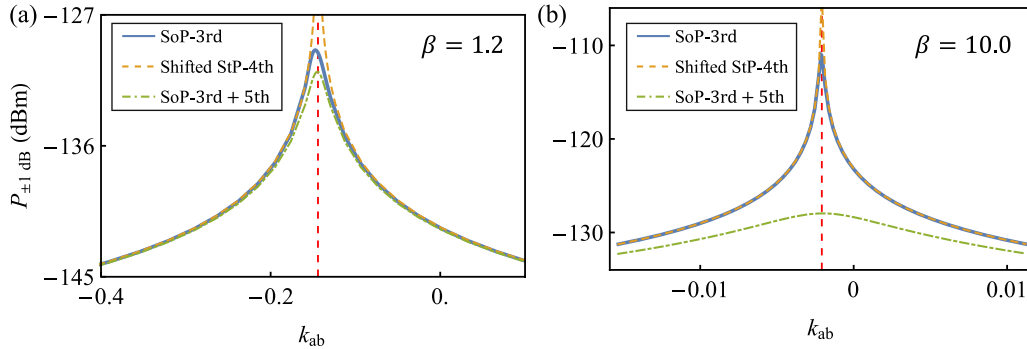

FIG. 6. We compare three different cases, soft pump with third-order coupling (SoP third), stiff pump with Kerr coupling (StP fourth), and soft pump truncated until the third order with fifth-order couplings between signal and idler mode (SoP third + fifth). For each cases, we manually turn on a cross-Kerr coupling k_{ab}. For StP fourth case, the plot is shifted by $-k_{ab}^{(\text{eff})}$. The vertical red dashed line shows the location where the real part of the dynamically generated cross-Kerr is fully compensated by the intrinsic cross-Kerr coupling. The parameters chosen: $\omega_a/(2\pi) = 7.5$ GHz, $\omega_b/(2\pi) = 5.0$ GHz, $\gamma_j/(2\pi) = 100$ MHz. We set $\beta = 1.2$ [in panel (a)] and 10.0 [in panel (b)]. The critical current is $i_c = 1.0 \mu$A.

SoP third line]. We observe that in both small β [see Fig. 6(a), $\beta = 1.2$] and large β [see Fig. 6(b), $\beta = 10.0$], as we tune the intrinsic Kerr term, the saturation power is maximized at the point indicated by the dashed red line. This maximum corresponds to the value of the intrinsic Kerr term that best cancels the generated Kerr coupling ($k_{ab} = -\text{Re}[k_{ab}^{\text{eff}}]$) and hence provides a maximum boost to the saturation power. We also notice that the maximum peak on Fig. 6(a) has a shift from the full compensation point ($k_{ab} = -\text{Re}[k_{ab}^{\text{eff}}]$). This is caused by the existence of imaginary term of f_{Σ}. In perturbation analysis, if we turn off the imaginary part of f_{Σ}, the peak is perfectly centered at the full-compensation point.

We also compare the saturation power obtained with SoP third order (blue solid lines) to the StP with intrinsic cross-Kerr term k_{ab} (orange dashed lines). In order to make the comparison more direct, we shift k_{ab} for the StP-Kerr amplifier by the computed value of the generated $\text{Re}[k_{ab}^{\text{eff}}]$ of the SoP third-order amplifier (i.e., we line up the peaks). We observe that away from the saturation power peak the two models are in good agreement, which supports the correspondence. Further, if we focus on $k_{ab} = 0$ point on the plot, i.e., the point at which SoP third-order model has no added intrinsic k_{ab}, the saturation power of SoP third-order amplifier (blue solid lines) matches the shifted StP cross-Kerr nonlinear amplifier (orange dashed lines) in both Figs. 6(a) and 6(b). Therefore, we conclude that it is indeed the generated Kerr coupling that is limiting the saturation power of the SoP third-order model.

However, near the saturation power maximum the two models diverge: the saturation power of the StP-Kerr amplifier becomes infinite as the intrinsic Kerr nonlinearity becomes zero, while the saturation power of the SoP third-order amplifier remains finite. This is caused by the imaginary part of k_{ab}^{eff} and the q_{ab}^{eff}, which cannot be compensated by a real intrinsic cross-Kerr coupling k_{ab}.

We can understand the $\text{Im}[k_{ab}^{\text{eff}}]$ and the q_{ab}^{eff} terms as a two-photon loss channel, i.e., in which a photon in the signal mode and a photon in the idler mode combine and are lost in the pump mode. Both of the terms can be mapped to an imaginary energy which represents the decay of the signal and idler mode fluxes. Specifically, $\text{Im}(f_{\Sigma})$ term represents the loss of a photon in signal mode and a photon in idler mode

to a pump photon with frequency $\omega = \Sigma$, while $\text{Im}(f_{\Delta})$ term represents the loss to a $\omega = \Delta$ pump photon.

E. Fifth and higher order nonlinearities

As we pointed out in Eq. (47), the saturation flux increases as we decrease the three-mode coupling strength g (by increase β). However, as we increase β, the saturation flux diverges from the SoP third-order model (see Fig. 3). This is because the saturation flux is so large that higher order nonlinear couplings becomes the limiting mechanism to the saturation flux. In this subsection, we focus on the higher order couplings and show how they limit the saturation flux of the amplifier.

At the Kerr nulling point, $\varphi_{\text{ext}} = 2\pi$, the Kerr couplings are turned off, and hence the next nonzero order of nonlinear couplings are fifth order in mode fluxes. The fifth-order terms in the expansion of the dimensionless potential energy of the JRM, Eq. (28), are

$$\mathcal{E}_{\text{JRM}}^{(5)} = h_a \varphi_a^3 \varphi_b \varphi_c + h_b \varphi_a \varphi_b^3 \varphi_c + h_c \varphi_a \varphi_b \varphi_c^3, \quad (50)$$

where $h_a = h_b = \frac{1}{24\beta} \sin\left(\frac{\varphi_{\text{ext}}}{4}\right)$ and $h_c = \frac{1}{6\beta} \sin\left(\frac{\varphi_{\text{ext}}}{4}\right)$. To understand the direct effects of the fifth-order couplings, we apply stiff-pump approximation and only include third- and fifth-order nonlinear coupling terms into the EOMs (Kerr couplings are turned off at $\varphi_{\text{ext}} = 2\pi$). Among the three fifth-order terms, h_a and h_b terms are more significant than h_c terms, because in stiff-pump approximation where the c mode is treated as stiff, the term $h_c \varphi_c^2 \varphi_a \varphi_b \varphi_c$ only shifts the pump mode flux to reach the desired gain G_0 and does not causes saturation. However, $h_a \varphi_a^2 \varphi_a \varphi_b \varphi_c$ and $h_b \varphi_b^2 \varphi_a \varphi_b \varphi_c$ terms dynamically shift the effective third-order coupling strength as we increase the input signal power, which saturates the amplifier.

Again, we apply perturbation theory to analyze the StP fifth-order amplifier following the discussion in Subsec. IV C. The lowest order solution of the signal and idler mode fluxes are at first order, which repeats the solution of the ideal parametric amplifier. The next nonzero correction appears at third order with equation $[M].[\varphi^{(3)}] = -[i].[\varphi_d^{(3)}]$, where $[i]$ is a 2×2 diagonal matrix with elements $\{i, -i\}$ and the corresponding drive term is

$$\left[\varphi_d^{(3)}\right] = \begin{pmatrix} 12 h_a \varphi_c |\varphi_a^{(1)}|^2 \varphi_b^{(1)*} + 6 h_a \varphi_c^* (\varphi_a^{(1)})^2 \varphi_b^{(1)} + 6 h_b \varphi_c |\varphi_b^{(1)}|^2 \varphi_b^{(1)*} \\ 6 h_a \varphi_c^* |\varphi_a^{(1)}|^2 \varphi_a^{(1)} + 12 h_b \varphi_c^* |\varphi_b^{(1)}|^2 \varphi_a^{(1)} + 6 h_b \varphi_c (\varphi_b^{(1)*})^2 \varphi_a^{(1)*} \end{pmatrix}. \quad (51)$$

In the high-gain limit, the third-order correction of the signal mode flux is

$$\varphi_a^{(3)} \sim 4 \frac{h}{g} \left(1 + \frac{\tilde{\gamma}_a}{\tilde{\gamma}_b}\right) G_0^2 \varphi_{a,\text{in}}^3, \quad (52)$$

where $h = h_a = h_b$ is the dimensionless fifth-order coupling strength. Following the same method, we get an estimate on the saturation flux

$$\varphi_{a,\text{in},\pm 1\text{dB}} \sim \sqrt{\epsilon \frac{g}{4h} \left(1 + \frac{\tilde{\gamma}_a}{\tilde{\gamma}_b}\right)} G_0^{-3/4}. \quad (53)$$

We note that the ratio g/h is independent of β. As we increase β to reduce the limitation placed by SoP third-order model, Eq. (47), we eventually hit the limit that is given by StP fifth-order nonlinear model, Eq. (53), i.e., the dominating limiting mechanisms on saturation flux switches.

To be more explicit, similar to the effective cross-Kerr compensation illustrated in Subsec. IV D, we add fifth-order nonlinear coupling terms into the SoP third-order nonlinear model, which is labeled as "SoP third + fifth" in Fig. 6 (green lines). In the small β regime [Fig. 6(a)], except around the generated cross-Kerr full compensation region, the SoP third + fifth-order nonlinear model closely follows the SoP

third-order model, especially at $k_{ab} = 0$ point where there is no intrinsic k_{ab} added to both of the models. This indicates that at low-β regime, the dominating limitation on the saturation power is given by the generated effective cross-Kerr coupling from the SoP third-order nonlinear coupling. However, when β is large [Fig. 6(b)], the saturation flux calculated from these two models disagrees. With additional fifth-order nonlinear couplings, the saturation flux is heavily suppressed, which shows that the fifth-order nonlinear couplings dominate the SoP third-order effects in limiting the saturation power of the amplifier.

Furthermore, in the large-β regime, the fifth-order nonlinear couplings in the JPA Lagrangian is the dominating limitation on the saturation power in full nonlinear EOMs of JPA among all the nonlinear couplings. To prove it, we numerically solve the saturation flux of the StP fifth-order truncated model of JPA ("StP fifth" line in Fig. 3) and compare it with saturation flux obtained from the full nonlinear EOMs ("all orders" line in Fig. 3). The saturation flux from StP fifth-order model matches the saturation flux of full nonlinear JPA model in large-β regime perfectly.

The saturation flux computed by numerical integration of StP fifth-order nonlinear model is independent of parameter β, which agrees with the perturbation analysis. To further validate the perturbation theory, we plot the saturation flux from third-order perturbation in Fig. 3(a) ("StP fifth third-order" line) for comparison. We notice that the perturbation result does not have a good quantitative agreement with the numerical solution. This is because the saturation flux is outside the radius of convergence of the perturbation series. If we tighten the criteria for amplifier saturation to the signal mode flux that causes the gain to change by ± 0.1 dB instead, the third-order perturbation on StP fifth has much better agreement with the numerical solutions [see Fig. 3(b) "StP fifth" line and "StP fifth third-order" line]. However, to perfectly match the numerical solution, we need next-order correction, i.e., fifth-order correction to signal mode flux. The result saturation flux is plotted in Fig. 3(b) as the red dot-dashed line.

Similarly, for the higher order nonlinear couplings in the Lagrangian, e.g., the seventh order in the Hamiltonian, we can still apply the perturbation theory to analyze the saturation flux. Here we focus on one of the seventh-order couplings, $-l_{aa}\varphi_a^4 \varphi_a \varphi_b \varphi_c$, to finalize the discussion. According to Eq. (12), l_{aa} is $\sin(\frac{\varphi_{ext}}{4})/(1920\beta)$. We still consider the truncated EOMs of the amplifier under stiff-pump approximation.

Following the same procedures discussed above, the lowest order solution of signal and idler mode fluxes are in first order and are given by the ideal parametric amplifier solution in Eq. (27). However, the next nonzero correction to signal and idler mode fluxes appears at fifth order with the corresponding drive term,

$$\left[\varphi_d^{(5)}\right] = 20\left|\varphi_a^{(1)}\right|^2 \begin{pmatrix} 3l_{aa}\left|\varphi_a^{(1)}\right|^2 \varphi_b^{(1)*}\varphi_c + 2\left(\varphi_a^{(1)}\right)^2 \varphi_b^{(1)} \varphi_c^* \\ l_{aa}\left|\varphi_a^{(1)}\right|^2 \varphi_a^{(1)} \varphi_c^* \end{pmatrix}.$$
(54)

The saturation flux given by this order of perturbation theory obeys

$$\varphi_{a,\text{in},\pm 1\text{dB}} \sim \left(\frac{g}{l_{aa}}\right)^{1/4} G_0^{-5/8}.$$
(55)

This limit does not depend on β either. With StP seventh-order truncated nonlinear model, where we include third-, fifth-, and seventh-order nonlinear couplings in JPA Lagrangian (even orders are turned off at $\varphi_{ext} = 2\pi$), the existence of the seventh-order nonlinear couplings contributes to a small correction to the saturation flux at large β. However, the fifth-order term remains the dominant factor in determining the saturation flux.

To conclude this section, for a JRM-based JPA that is operated at the nulling point with fixed mode frequencies and mode linewidth, saturation flux can be increased by increasing β, which suppresses the effects of generated Kerr couplings. As we move to large-β regime, if we want to further improve the saturation power of the amplifier, we need to reduce the fifth- and higher order nonlinear coupling strengths with respect to the third-order coupling strength in the Lagrangian. In Ref. [24], we notice that the imperfect participation ratio $p \neq 1$ caused by nonzero linear inductance in series of JRM circuit is one of the candidates for the suggested suppression, which will be discussed in the following sections.

V. EFFECTS OF PARTICIPATION RATIO

In this section, we focus on the effects of reducing participation ratio by introducing outer linear inductors in series with the JRM circuit [L_{out} in Fig. 7(a)].

When there are external resonators connected to the JRM, the flux injected from the microwave ports is shared between the JRM and the external resonators and hence the JRM nonlinearity is attenuated. To model this effect, four outer linear inductors L_{out} are added in series with the JRM circuit [see Fig. 7(a)]. These inductors and the JRM can be treated as a "flux-divider" type of circuit. Further, as the input-output ports are connected to the outer nodes and there is no capacitors connecting the inner nodes to ground, we treat the fluxes of outer nodes ($\tilde{\varphi}_j$) as free coordinates, while the inner node fluxes (φ_j) are restricted by the Kirchhoff's current relation. The potential energy of JRM becomes

$$E = E_{out} + E_{JRM}$$
$$= \sum_j \frac{\phi_0^2}{L_{out}} (\tilde{\varphi}_j - \varphi_j)^2 + E_{JRM}(\varphi_1, \varphi_2, \varphi_3, \varphi_4).$$
(56)

The EOM for node flux $\tilde{\varphi}_j$ are

$$\ddot{\tilde{\varphi}}_j + \frac{1}{C_j L_{out}} (\tilde{\varphi}_j - \varphi_j) = \tilde{I}_{in,j},$$
(57)

where $j = 1, 2, 3, 4$ and the node capacitance $C_j = C_a$ for $j = 1, 3$ and $C_j = C_b$ for $j = 2, 4$. The right hand side, $\tilde{I}_{in,j}$, is the corresponding input terms derived in Eq. (19) for each node flux. The inner node fluxes φ_j are restricted by

$$\tilde{\varphi}_j = \varphi_j + \zeta\left[\frac{1}{\beta}\sin\left(\varphi_j - \varphi_{j+1} + \frac{\varphi_{ext}}{4}\right)\right.$$

$$\left. - \frac{1}{\beta}\sin\left(\varphi_{j-1} - \varphi_j + \frac{\varphi_{ext}}{4}\right) + \frac{1}{4}\left(3\varphi_j - \sum_{k\neq j}\varphi_k\right)\right],$$
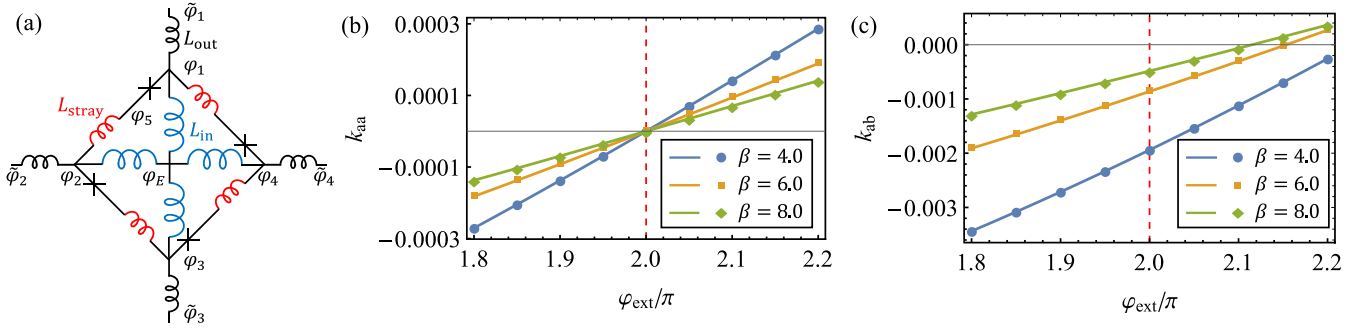(58)

FIG. 7. In panel (a), we show a more realistic circuit model for JRM, in which we include stray inductance L_{stray} in series of Josephson junctions and outer linear inductance L_{out} in series of JRM. The fluxes associated with each nodes are labeled on the plot. In panels (b) and (c), we calculate the Kerr coupling strength k_{aa} (b) and k_{ab} (c) as we sweep external magnetic field bias φ_{ext} when participation ratio $1/p = 1.1$. The perturbation solution (lines) and numerical solution (dots) agree well. In panel (b), for all three β values, the self-Kerr coupling strength k_{aa} can always be turned off at the Kerr nulling point $\varphi_{\text{ext}} = 2\pi$. However, in panel (c), we notice that the magnetic field bias φ_{ext} to turn off cross-Kerr coupling k_{ab} depends on the choice of β. This means the exact Kerr nulling point of the does not exist any more when the participation ratio is not unity. Parameters chosen: three mode decay rates are $\gamma/(2\pi) = 0.1$ GHz, the critical current of the junctions is $i_c = 1.0$ μA. The outer linear inductance ratio $\zeta = 0.1$. The rest of the circuit elements are set by the mode frequencies at $\varphi_{\text{ext}} = 2\pi$, and they remains when we tune the external flux bias.

where $\zeta = L_{\text{out}}/L_{\text{in}}$ and we apply index conventions that $\varphi_0 = \varphi_4$ and $\varphi_5 = \varphi_1$. As the symmetry of the JRM still persists, the normal mode profiles in terms of the outer node fluxes $\tilde{\varphi}$'s are identical to the ones without outer linear inductance; i.e., the normal mode coordinates are given by $[\tilde{\varphi}_M] = [\mathcal{A}^{-1}].[\tilde{\varphi}]$, where the model matrix $[\mathcal{A}]$ is identical to Eq. (8). This can also be derived from the linearization of the JPA's EOMs [Eq. (57)] and the constraints in Eq. (58). But the frequencies of the normal modes are shifted,

$$\omega_{a,(b)}^2 = \frac{1}{2C_{a,(b)}L_{\text{in}}} \frac{\beta + 2\cos\left(\frac{\varphi_{\text{ext}}}{4}\right)}{\beta + \beta\zeta + 2\zeta\cos\left(\frac{\varphi_{\text{ext}}}{4}\right)}, \quad (59a)$$

$$\omega_c^2 = \frac{1}{C_c L_{\text{in}}} \frac{\beta + 4\cos\left(\frac{\varphi_{\text{ext}}}{4}\right)}{\beta + \beta\zeta + 4\zeta\cos\left(\frac{\varphi_{\text{ext}}}{4}\right)}, \quad (59b)$$

where $C_c = \frac{4C_a C_b}{C_a + C_b}$.

The question of how the nonlinear couplings shift when we add L_{out} into the JRM circuit is hard to directly analyze by the expanding the JRM potential energy in terms of normal modes around the ground state, as the constraints [Eq. (58)] are hard to invert. To obtain the nonlinear coupling strengths, we can either numerically calculate the derivatives of the potential energy with respect to the mode fluxes or using analytical perturbation expansion to get an approximate inversion relation of Eq. (58) and find the nonlinear couplings. Here we stop at fourth-order nonlinearities (in energy).

To solve the self-Kerr k_{jj} and cross-Kerr k_{ij} nonlinear coupling strengths, we can calculate the fourth-order derivatives of the circuit potential energy E with respect to the normal coordinates $\tilde{\varphi}_a$, $\tilde{\varphi}_b$, and $\tilde{\varphi}_c$, i.e.,

$$k_{jj} = \frac{1}{24} \frac{\partial^4 \mathcal{E}}{\partial \tilde{\varphi}_j^4}, \quad k_{ij} = \frac{1}{4} \frac{\partial^4 \mathcal{E}}{\partial \tilde{\varphi}_i^2 \partial \tilde{\varphi}_j^2}, \quad (60)$$

where $\mathcal{E}$ is dimensionless energy of JRM circuit defined as $\mathcal{E} = (L_{\text{in}}/\phi_0^2)E$.

It is straightforward to use inner node fluxes to express the energy E in Eq. (56) and hence find an analytical expression for the derivatives with respect to inner node fluxes. However,

to calculate derivatives with respect to the outer node fluxes requires the Jacobian matrix $[J] = [\frac{\partial \varphi}{\partial \tilde{\varphi}}]$, which effectively requires inversion of the constrains in Eq. (58).

To analytically solve this problem and give us a hint on how the outer linear inductance will affect the nonlinear couplings, we apply the perturbation expansion around the ground state ($\tilde{\varphi}_j = 0$) to obtain an approximate inverse transformation and find the Jacobian. To simplify the discussion, we assume $C_a = C_b$. We note that this assumption does not affect the nonlinear coupling strengths which are independent of the c mode. Further, the method we discussed below can be easily generalized to the case when $C_a \neq C_b$.

We at first define a set of new variables using the normal mode transformation matrix $[\mathcal{A}]$, but use the inner node fluxes instead, noted as $[\varphi_M] = [\mathcal{A}^{-1}].[\varphi]$. Therefore, the relation in Eq. (58) using normal coordinates $[\tilde{\varphi}_M]$ and inner node coordinates $[\varphi_M]$ is

$$\tilde{\varphi}_j = (1+\zeta)\varphi_j + (2)\frac{2\zeta}{\beta}\frac{\partial}{\partial \varphi_j}\mathcal{E}_{\text{JRM}}^{(0)}, \quad (61)$$

where $\mathcal{E}_{\text{JRM}}^{(0)}$ is given in Eq. (28), the factor (2) only exists for a and b modes. Here we only focus on the three nontrivial modes, $\tilde{\varphi}_a$, $\tilde{\varphi}_b$, and $\tilde{\varphi}_c$. The circuit ground state is assumed to be stable and at $\tilde{\varphi}_a = \tilde{\varphi}_b = \tilde{\varphi}_c = 0$ (which we confirm numerically). Further, at this stable ground state, the inner node fluxes are also zero. Since we only focus on the Kerr coupling strength in the vicinity of the ground state, the exact inner node fluxes that obey the inverse relation of Eq. (61) can be expanded in series of the small oscillations of the normal modes $\tilde{\varphi}_j$'s. That is, $\varphi_j \sim 0 + \varphi_j^{(1)} + \varphi_j^{(2)} + \dots$.

We plug the expansion of inner node fluxes back to Eq. (58) and match the terms with order by order. The lowest order solutions appear at the first order in normal coordinates

$$\varphi_{a,b}^{(1)} = \left[1 + \zeta + \frac{2\zeta}{\beta}\cos\left(\frac{\varphi_{\text{ext}}}{4}\right)\right]^{-1}\tilde{\varphi}_{a,b}, \quad (62a)$$

$$\varphi_c^{(1)} = \left[1 + \zeta + \frac{4\zeta}{\beta}\cos\left(\frac{\varphi_{\text{ext}}}{4}\right)\right]^{-1}\tilde{\varphi}_c. \quad (62b)$$

At this order, we can extract the definition of participation ratio for signal and idler mode as $p_{a,b} = [1 + \zeta + \frac{2\zeta}{\beta}\cos(\frac{\varphi_{\text{ext}}}{4})]^{-1}$ and for pump mode as $p_c = [1 + \zeta + \frac{4\zeta}{\beta}\cos(\frac{\varphi_{\text{ext}}}{4})]^{-1}$. If we bias the circuit at $\varphi_{\text{ext}} = 2\pi$, all three participation ratios become $p_0 = \frac{1}{1+\zeta}$.

The second-order correction to the inner node fluxes are

$$\varphi_a^{(2)} = p_a \frac{2\zeta}{\beta} \sin\left(\frac{\varphi_{\text{ext}}}{4}\right)\varphi_b^{(1)}\varphi_c^{(1)}, \tag{63a}$$

$$\varphi_b^{(2)} = p_b \frac{2\zeta}{\beta} \sin\left(\frac{\varphi_{\text{ext}}}{4}\right)\varphi_b^{(1)}\varphi_c^{(1)}, \tag{63b}$$

$$\varphi_c^{(2)} = p_c \frac{\zeta}{\beta} \sin\left(\frac{\varphi_{\text{ext}}}{4}\right)\varphi_a^{(1)}\varphi_b^{(1)}. \tag{63c}$$

The corresponding approximate inverse transformation of Eq. (58) is $\varphi_j \sim \varphi_j^{(1)}(\{\tilde{\varphi}\}) + \varphi_j^{(2)}(\{\tilde{\varphi}\})$ for $j = a, b, c$. At second order, it is sufficient to calculate the three-mode coupling

strength, as we only need at most the second-order derivatives to the Jacobian matrix elements. The dimensionless three-mode coupling strength is

$$g(\zeta) \equiv \frac{\partial^3 \mathcal{E}}{\partial\tilde{\varphi}_a\partial\tilde{\varphi}_b\partial\tilde{\varphi}_c} = p_a p_b p_c g(0), \tag{64}$$

where $g(0)$ is the three-mode coupling strength with unit participation ratio. Based on Eq. (64), decreasing the participation ratio by increasing L_{out} reduces the corresponding third-order coupling strength, which is beneficial to reduce the limitation placed by the effective cross-Kerr nonlinearity generated by SoP third-order nonlinear couplings, and hence it is beneficial to improving the saturation power of the amplifier in the small β regime.

However, to calculate the fourth-order derivatives, we need at least third-order correction to the inner node fluxes. Following the same strategy, the third-order correction of the inverse transformation for normal coordinate φ_a is

$$\varphi_a^{(3)} = \frac{p_a^4 \zeta}{12\beta}\cos\left(\frac{\varphi_{\text{ext}}}{4}\right)\tilde{\varphi}_a^3 + \frac{p_a^2 p_b^2 \zeta}{4\beta^2}\left[\beta\cos\left(\frac{\varphi_{\text{ext}}}{4}\right) + 8p_c\zeta\sin^2\left(\frac{\varphi_{\text{ext}}}{4}\right)\right]\tilde{\varphi}_a\tilde{\varphi}_b^2$$
$$+ \frac{p_a^2 p_c^2 \zeta}{4\beta^2}\left[\beta\cos\left(\frac{\varphi_{\text{ext}}}{4}\right) + 4p_b\zeta\sin^2\left(\frac{\varphi_{\text{ext}}}{4}\right)\right]\tilde{\varphi}_a\tilde{\varphi}_c^2 \tag{65}$$

and the relations for $\varphi_b^{(3)}$ and $\varphi_c^{(3)}$ can be derived similarly. The inverse relation from Eq. (58) is $\varphi_j \sim \varphi_j^{(1)}(\{\tilde{\varphi}\}) + \varphi_j^{(2)}(\{\tilde{\varphi}\}) + \varphi_j^{(3)}(\{\tilde{\varphi}\})$. The Kerr coupling strengths can be obtained from Eq. (60) with Jacobian derived from the perturbation expansion. For example, k_{ab} is

$$k_{ab}(\zeta) = -\frac{\beta^3\{\beta(1+\zeta)\cos\left(\frac{\varphi_{\text{ext}}}{4}\right) + 2\zeta\left[-3 + \cos\left(\frac{\varphi_{\text{ext}}}{4}\right) + 8\sin\left(\frac{\varphi_{\text{ext}}}{4}\right)\right]\}}{16\left[\beta + \beta\zeta + 2\zeta\cos\left(\frac{\varphi_{\text{ext}}}{4}\right)\right]^4\left[\beta + \beta\zeta + 4\zeta\cos\left(\frac{\varphi_{\text{ext}}}{4}\right)\right]}. \tag{66}$$

The self-Kerr coupling strength k_{aa} and the cross-Kerr coupling strength k_{ab} are plotted in Figs. 7(b) and 7(c), respectively. The Kerr nonlinear coupling strengths (k_{aa} and k_{ab}) are calculated via both numerical method (dots) and the above perturbation method (lines). In all three β values, the perturbation analysis matches the numerical solution well. Further, we notice that the self-Kerr coupling strength can still be turned off at the $\varphi_{\text{ext}} = 2\pi$ (Kerr nulling point) no matter what β value we choose [see Fig. 7(b)]. But the cross-Kerr couplings cannot be turned off at this magnetic bias point when participation ratio is not unity [see Fig. 7(c)].

The breakdown of the universal Kerr nulling point is also demonstrated by Eq. (66). The φ_{ext} that makes the numerator of Eq. (66) zero depends on the choice of β and ζ. This indicates that as we turn the participation ratio to be smaller than unity, some nonlinear couplings that are previously killed by Kerr nulling point can reappear in the JPA Lagrangian. These extra nonlinear couplings are a consequence of the nonlinearity of the inner JRM circuit. As we mentioned, the JRM circuit with outer linear inductance shown in Fig. 7(a) can be treated as a phase divider; i.e., the phase across the outer nodes is divided by the phase across the outer linear inductors (L_{out}) and the phase across the inner JRM nodes governed by the effective inductance of the inner JRM. Naively, if the divider is linear, we would expect the JRM with outer linear inductance generates nonlinear coupling strengths that are

suppressed by the participation ratio (which does not depend on the mode flux); e.g., $k_{ab}(\zeta) = p_a^2 p_b^2 k_{ab}(0)$ and $k_{ab}(0) = 0$ is the cross-Kerr coupling strength of a JRM without outer linear inductance. However, as the effective inductance of inner JRM circuit is nonlinear, the total phase is not divided linearly, i.e., the more precise participation ratio defined as $p = \tilde{\varphi}/\varphi$ will change as the input flux oscillates as it is indeed a function of the outer node fluxes. Therefore, the normal modes experience extra nonlinearities as compared to the naive analysis. The reappearance of these extra nonlinearities will limit the saturation power of the amplifier.

However, for a general φ_{ext}, the Kerr couplings are suppressed roughly by $\sim p^4$. If we calculate one order up, the fifth-order nonlinear coupling strength is suppressed by $\sim p^5$. This indicates that the nonunity participation ratio can help to suppress the higher order nonlinear couplings with respect to the third order, which is beneficial for improving the saturation power of the amplifier. We will focus on the quantitative understand of how these two factors compete with each other and further optimize the saturation power of the amplifier in next section.

VI. OPTIMIZING THE JPA USING PARTICIPATION RATIO

As demonstrated in the above section, the outer linear inductance impacts the saturation power of the JPA in both

negative and positive ways. In this section, we describe the effects of the outer linear inductance quantitatively using numerics to obtain the saturation power of the JPA as we sweep the JRM inductance ratio (β) and participation ratio (p).

Because of the presence of the outer linear inductance, even order nonlinear coupling terms reappears in the EOMs. The presence of these higher order couplings results in a shift of the mode frequencies. For example, the nonzero cross-Kerr coupling strength $k_{ac}\varphi_a^2\varphi_c^2$ and $k_{bc}\varphi_b^2\varphi_c^2$ causes the signal and idler mode frequencies to be dependent on the pump mode strength, which shifts the signal and idler mode frequencies away from the bare mode frequencies calculated from the normal mode analysis. To correctly pump the amplifier with the sum frequency of mode and idler mode frequencies and probe the signal with the correct signal mode frequency, as well as set the amplifier's small-signal reflection gain to 20 dB, we need to adjust the pump tone frequency and pump tone strength at the same time. Before we perform the numerical calculation of the amplifier's reflection gain as we tune the input tone strength and extract the saturation power, we need to find the correct pump configurations and the signal mode frequency under that pump configuration.

To compensate for the frequency shifts and find the optimum pump configuration and corresponding signal mode frequency for JPA, we numerically optimize the pump tone frequency and strength. To solve this optimization problem, we notice that the amplifier is expected to consume the least pump tone input flux to reach the desired small-signal reflection gain when the amplifier is perfectly on resonance with its mode frequencies, i.e., $\omega_S = \omega_a$ and $\omega_P = \omega_a + \omega_b$. Therefore, we split the optimization process into two optimization tasks: (1) for a given input pump tone strength $\varphi_{c,\text{in}}$, find the optimimal pump tone frequency and signal mode frequency and (2) find the desired pump tone strength $\varphi_{c,\text{in}}$ to get 20 dB small-signal reflection gain with the corresponding optimized pump tone frequency. In (1), we fix the pump tone strength $\varphi_{c,\text{in}}$ and sweep signal tone and pump tone frequencies to find the parameters which maximize the reflection gain (a typical sweep is shown in Fig. 8). In (2), we use a binary search to find the desired pump strength $\varphi_{c,\text{in}}$ for 20 dB reflection gain.

The resulting saturation power sweep of the JPA is shown in Fig. 1(a). In the large-β regime ($\beta > 4.0$), as we decrease the participation ratio, the saturation power increases. However, at the same time, the pump power for 20-dB reflection gain also increase, until the JRM reaches the full nonlinear regime and we cannot inject enough power to get 20-dB reflection gain anymore. However, in the low-β regime ($\beta < 4.0$), when the participation ratio is less than unity, even though we first optimize the pump configuration to compensate for mode shifting, we still found that the reflection gain of the amplifier increases before it starts to drop ("shark fin"). This causes the amplifier to saturate as gain increases to 21 dB. If we move out of this regime by reducing the participation ratio or increase β, the "shark fin" reduces and we find a band of sweet spots of the JPA saturation power. The reflection gain of the JPA with configurations around one of the sweet spots is shown in Fig. 9(a), with the the blue curve corresponding to the sweet spot at $\beta = 3.5$, $1/p = 7.0$. As we decrease β to 3.0, the JPA saturates as gain touches 21 dB [green dash-dotted
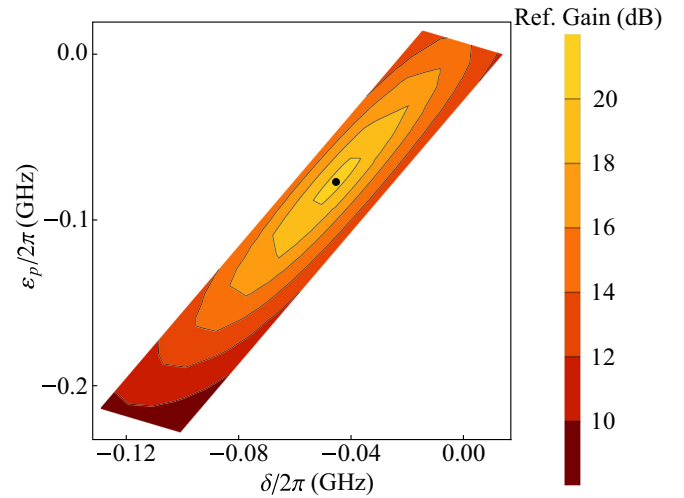

FIG. 8. The optimization of the pump configuration. We sweep the signal mode detuning $\delta = \omega_S - \bar{\omega}_a$ and the pump tone detuning $\epsilon_p = \omega_P - (\bar{\omega}_a + \bar{\omega}_b)$ and fix the pump tone strength. The maximum gain is labeled by the black dot. The maximum gain is achieved when the signal tone matches the mode frequency and the pump mode matches the sum frequency of the signal and idler mode. The parameters used: $\gamma/2\pi = 0.2$ GHz, $\bar{\omega}_a/2\pi = 7.5$ GHz, $\bar{\omega}_b/2\pi = 5.0$ GHz, $\beta = 3.0$, $1/p = 8.0$.

curve in Fig. 9(a)], while as we increase β to 4.0 the "shark fin" disappears but the saturation power decreases.

To understand the dominating limitations placed by different nonlinear terms in the JPA Hamiltonian, especially around the sweet spot, we truncate the Hamiltonian order by order and analyze the performance of the truncated model. We keep the pump configurations identical to the full-order analysis and increase the truncation order from third order to eighth order. In Fig. 9(b), we focus on the sweet spot $\beta = 3.5$, $1/p = 7.0$, and compare the truncated theory with the full-nonlinear solution. At small signal input, the nonlinear couplings up to secventh order are needed to converge to the desired 20-dB reflection gain. This is a sign that the high-order nonlinear coupling terms play an important role in the dynamics of the JPA. As we increase the signal power, the truncation to fourth-order analysis does not show an obvious "shark fin" feature. However, when we include the higher order coupling terms, e.g., fifth to eighth, the "shark fin" appears. The truncated fifth-order analysis supports another mechanism that causes the amplifier to saturate to 21 dB which is different from the one discussion in Ref. [24]; that is, the fifth-order terms, e.g., $\varphi_a^2\varphi_a\varphi_b\varphi_c$ term, can shift the bias condition by shifting the effective third-order coupling strength to drive the amplifier toward the unstable regime, causing the reflection gain to rise. Further, as we discussed above, the external linear inductors break down the perfect nulling point for even order nonlinear couplings; the sixth-order and eighth-order terms can survive at the nulling point. From fifth- order to eighth-order truncation, the large signal input behavior oscillates, which is a sign that we are reaching the convergence point of the series expansion caused by the competition between different orders. We also compare it with a point away from the sweet spot in Fig. 9(c) ($\beta = 3.5$, $1/p = 4.0$). At this point, the fifth-order
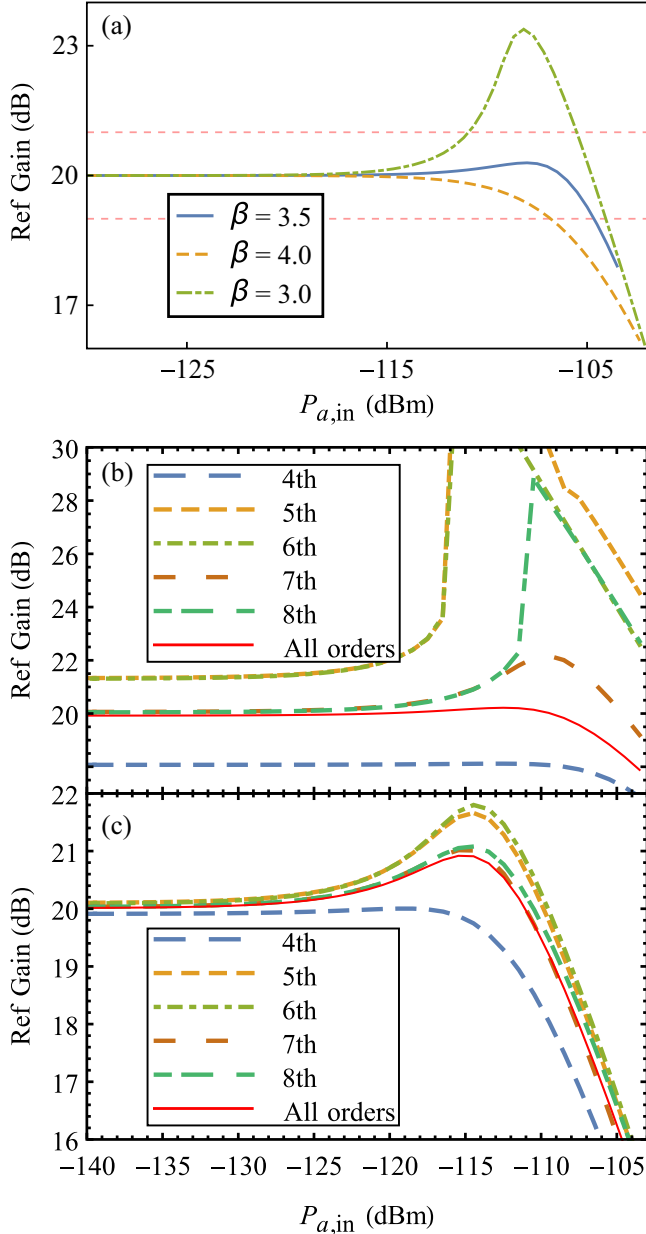
FIG. 9. In this plot, we show the reflection gain of the amplifier as we increase the input signal power. We focus on a point which is away from the boundary shown in Fig. 7(a). We test the reflection gain of the truncated model for $\beta = 4.5$ and $1/p \sim 4.0$ as we increase the input signal power $P_{a,\text{in}}$ in panel (c). In the calculation for the truncated model, we only truncate the JRM potential energy to the desired order, but fix the pump configuration as the full-order case. The reflection gain solved from truncated model also converge to the full-order analysis (red solid line) pretty well we truncated to seventh order. But as we decrease p further to push the configuration closer to the boundary ($1/p = 7.0$), the higher order terms are needed to have a good approximation to the full-order performance.

truncation already converges to 20-dB reflection gain and the seventh-order theory gives a good approximation to full order analysis with moderate input signal power. We conclude that the boost in performance of the amplifier at the sweet spot is

a result of taking advantage of all orders, and hence cannot be modeled using a low-order truncated theory.

VII. EFFECTS OF TUNING THE EXTERNAL MAGNETIC FIELD, DECAY RATES, AND STRAY INDUCTANCE

In this section, we further explore how the saturation power of the amplifier is affected by the magnetic field bias (φ_{ext}), the modes' decay rates (γ), and stray inductance in the JRM loop [L_{stray} in Fig. 7(a)].

In Fig. 10, we plots the saturation power of the amplifier as we perturb the magnetic field bias and decay rates of JPA. Here we focus on the line of $1/p = 7.0$ in Figs. 10(a) and 10(b), and focus on the line of $\beta = 3.5$ in Figs. 10(c) and 10(d). In Figs. 10(a) and 10(c), we explore the effects of tuning the magnetic field bias. We at first set the JPA circuit parameters at $\varphi_{\text{ext}} = 2\pi$. We then operate the JPA at $\varphi_{\text{ext}} = 1.9\pi$ and $\varphi_{\text{ext}} = 2.1\pi$, respectively. We notice that as we perturb the magnetic field to $\varphi_{\text{ext}} = 1.9\pi$, the optimum saturation power is achieved at larger β values [see Fig. 10(a)] and smaller participation ratio p [see Fig. 10(c)]. By tuning β, the saturation power of the amplifier improves from -104.8 to -103.9 dB m, while by tuning p, it improves to -104.1 dB m. This indicates that the optimal magnetic field bias occurs at somewhat lower magnetic field as compared to the Kerr nulling point. The corresponding sweet spot of the amplifier has larger β and lower p compared to the present setting.

In Figs. 10(b) and 10(d), we change the JPA modes' decay rates by 10 MHz to explore the effects of different decay rates on the JPA saturation power. In the large-β regime, increasing the JPA mode decay rates causes the regime in which we cannot obtain 20-dB (see Fig. 1) gain to become larger. For example, at $\gamma/2\pi = 0.21$ GHz, the JPA with $\beta = 6.0$ and $1/p = 7.0$ can no longer reach 20-dB reflection gain while a comparable JRM with $\gamma/2\pi = 0.20$ GHz could. The amplifier's optimum saturation power is also achieved at a lower β value as we increase the decay rates [see Fig. 10(b)]. However, as we tune the decay rates by ± 10 MHz, the maximum saturation power of the amplifier at $1/p = 7.0$ shows little change. Similarly, in Fig. 10(d), we perturb the modes' decay rates by ± 10 MHz on JPA with different p but a fixed β ($\beta = 3.5$). The amplifier's optimum saturation power is achieved at a lower p value as we decrease the decay rates [see Fig. 10(d)], while the maximum saturation power of the amplifier still shows little change.

Finally, we consider the effect of stray inductors (L_{stray} in Fig. 7). We include stray inductance such that $\alpha = L_{\text{stray}}/L_J = 0.1$ and compare the reflection gain of the amplifier as we increase the signal power (P_a). Note that when the stray inductance is nonzero, the Kerr nulling point is shifted away from $\varphi_{\text{ext}} = 2\pi$ (see discussion in Subsec. A 1), and especially that when $\alpha = 0.1$, the Kerr nulling point is at $\varphi_{\text{ext}} \sim 2.49\pi$. We will operator the JPA at this magnetic field bias when the participation ratio is not unity. In Fig. 11, we compare three different settings of JPA, $1/p = 7.0$, $\beta = 3.0$ (blue curves), $1/p = 7.0$, $\beta = 3.5$ (orange curves), and $1/p = 7.0$, $\beta = 4.0$ (green curves). In all three different sittings, we notice enhancement of the "shark fin," which causes the JPA at the previous sweet spot ($\beta = 3.5$, orange dashed curve) saturates to 21 dB instead, which greatly reduce the saturation power at
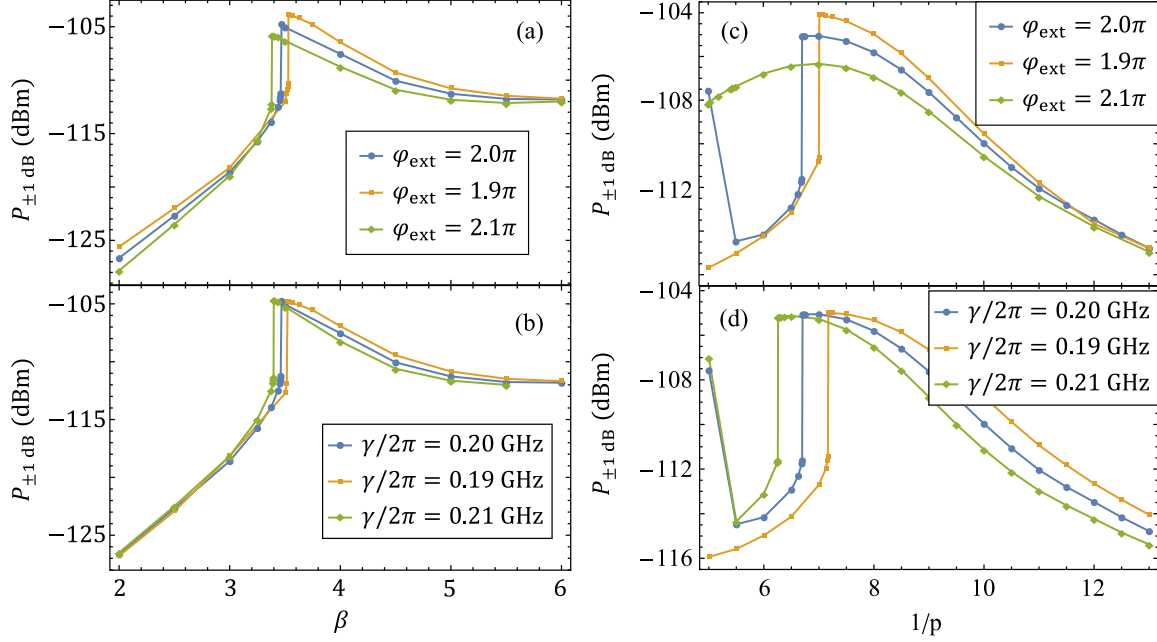
FIG. 10. The saturation power of the JPA with external magnetic field bias and mode decay rates' perturbation. In panels (a) and (c), we perturb the JPA external magnetic field bias from 2π by $\pm 0.1\pi$. We assume the JPA circuit parameters are fixed with bias $\varphi_{\text{ext}} = 2\pi$, and then we operate the JPA at the perturbed magnetic field bias. In panels (b) and (d), we set the circuit parameters of JPA to change the modes' decay rates from $\gamma/2\pi = 0.2$ GHz by ± 10 MHz. In panels (a) and (b), we focus on the JPA settings with $1/p = 7.0$ and investigate the effect of the perturbation, while in panels (c) and (d), we focus on the settings with $\beta = 3.5$.

this point (from -104.8 to -120 dB m). At $\beta = 4.0$, without stray inductors, the reflection gain of the amplifier monotonically decreases as the signal power increases (dashed green line), while at $\alpha = 0.1$ there is a shallow increases (see solid green line). Besides, the saturation power slightly drops from -107.5 to -108.7 dB m.
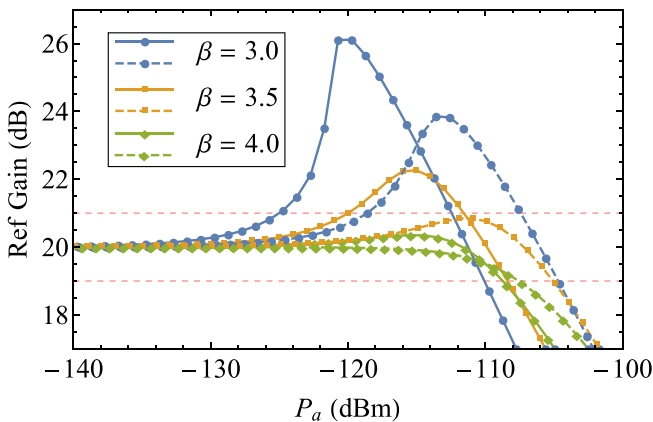

FIG. 11. We compare the saturation power of the amplifier without stray inductance ($\alpha = 0$, dashed curves) and with stray inductance ($\alpha = 0.1$ slide curves). We tested three different settings of JPA, $\beta = 3.0$, 3.5, and 4.0, respectively. All of them have $1/p = 7.0$. We compare the reflection gain of the amplifier as we increase the signal power P_a. For all three cases, the saturation power is suppressed. The existence of the stray inductance enhances the shark fin, which causes the amplifier at previous sweet spot ($1/p = 7.0$ and $\beta = 3.5$) saturates to 21 dB instead.

VIII. SUMMARY AND OUTLOOK

In conclusion, we have investigated the nonlinear couplings of the JRM-based JPA and how these different nonlinear couplings control the performance of the parametric amplifier. In our analysis, we have adapted both perturbative and time-domain numerical methods to give us a full understanding of the circuit dynamics. By considering the full nonlinear Hamiltonian of the device, we show that we can fully optimize the performance of the amplifier, and achieve an ≈ 10 to 15 dB improvement of the saturation power of the JRM-based JPA for a range of circuit parameters. Our method for numerically modeling multiport circuits of inductors, capacitors, and Josephson junctions is also applicable to more complex circuits and pumping schemes, which can create JPAs with addition virtues such as extremely broad (and gain-independent) bandwidth and directional amplification [15,17,18,32,42,43].

APPENDIX

1. The effect of stray inductance with unit participation ratio

In this section, we focus on the effect of the existence of nonzero stray inductance with unit participation ratio. This discussion is also provided in Ref. [17].

The circuit model of JRM circuit with stray inductance is in Fig. 7(a). When the stray inductance is nonzero, similar to shunted JRM circuit, we can write the potential energy of JRM circuit as

$$E_{\text{JRM}} = \frac{\phi_0^2}{2L_{\text{in}}} \sum_j (\varphi_j - \varphi_E)^2 + \sum_j E_{\text{arm}}(\delta_j), \quad \text{(A1)}$$

where $\varphi_E = \frac{1}{4}(\varphi_1 + \varphi_2 + \varphi_3 + \varphi_4)$, the arm energy, E_{arm}, is the total energy of the stray inductor and the Josephson junction on one arm of the JRM, $\delta_j = \varphi_j - \varphi_{j+1} + \frac{\varphi_{\text{ext}}}{4}$ is the total phase difference across the jth arm. Take one of the arms as an example:

$$H_{\text{arm}}(\delta_1) = \frac{\phi_0^2}{2L_{\text{stray}}} (\varphi_1 - \varphi_5)^2 - \frac{\phi_0^2}{L_J} \cos\left(\varphi_5 - \varphi_2 + \frac{\varphi_{\text{ext}}}{4}\right), \quad \text{(A2)}$$

where the phase on node φ_5 is constrained by the current relation at the corresponding node,

$$\delta_1 - \Delta\varphi = \alpha \sin(\Delta\varphi), \quad \text{(A3)}$$

where $\alpha = L_{\text{stray}}/L_J$, $\delta_1 = \varphi_1 - \varphi_2 + \frac{\varphi_{\text{ext}}}{4}$ is the total phase difference of the arm and $\Delta\varphi$ is the phase across the junction, defined as $\Delta\varphi = \varphi_5 - \varphi_2 + \frac{\varphi_{\text{ext}}}{4}$. Suppose we focus on the case where the external magnetic flux is around 2π, when α is small ($\alpha < 2.80$); then the nonlinear relation in Eq. (A3) only has a single root when the total phase across the arm is determined.

To determine the self-Kerr k_{jj} and cross-Kerr k_{ij} coupling strengths, we can use the derivatives of the dimensionless JRM energy as

$$k_{jj} = \frac{1}{24} \frac{\partial^4 \mathcal{E}_{\text{JRM}}}{\partial \varphi_j^4}, \quad k_{ij} = \frac{1}{4} \frac{\partial^4 \mathcal{E}_{\text{JRM}}}{\partial \varphi_i^2 \partial \varphi_j^2}. \quad \text{(A4)}$$

Before we carry on the derivative, we appreciate the facts that the phase difference across the arms are linearly dependent on the node fluxes and the node fluxes are linearly dependent on the normal mode coordinates. Since the inner linear inductance only contributes the energy which is quadratic to the node phases, there will be no contribution to the Kerr couplings. Because the four arms of the JRM are symmetric, the arm Hamiltonian for four arms should have identical form
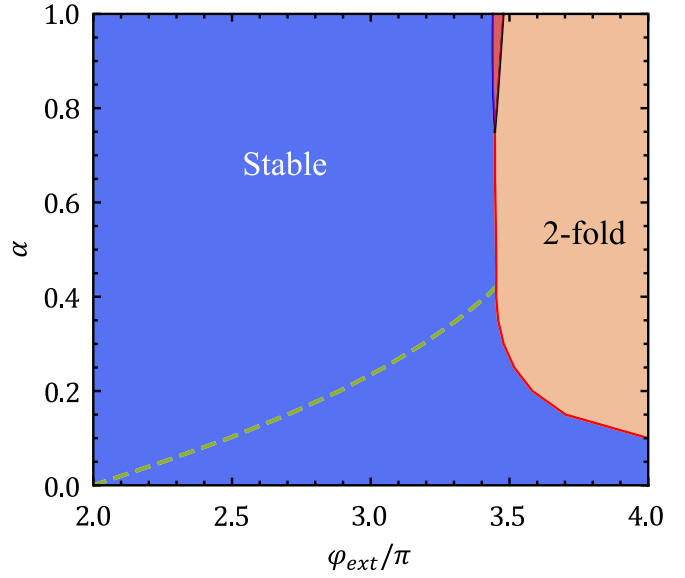

FIG. 12. The stability diagram of the ground state of the JPA when we have nonzero stray inductance. We assume $L_{\text{out}} = 0$ and set $\beta = 4.0$. The blue region (labeled as "stable") shows the stable region of the JPA ground state, while in the orange region (labeled as "2-fold"), the JPA ground state is doubly degenerate. In the red region (unlabeled region), JPA has a fourfold degenerate ground state. The green line shows the position of the nulling point.

in terms of the phase difference δ. To finalize the calculation, the fourth-order derivatives with respect to normal modes in general can be calculated as

$$\frac{\partial^4}{\partial \varphi_i^2 \partial \varphi_j^2} \mathcal{E}_{\text{JRM}} = \sum_l \frac{\partial^4}{\partial \varphi_i^2 \partial \varphi_j^2} \mathcal{E}_{\text{arm}}(\delta_l)$$

$$= \sum_l \left(\frac{\partial^4}{\partial \delta^4} \mathcal{E}_{\text{arm}}\right) \left(\frac{\partial \delta_l}{\partial \varphi_i}\right)^2 \left(\frac{\partial \delta_l}{\partial \varphi_j}\right)^2. \quad \text{(A5)}$$

Therefore, for both self-Kerr couplings and cross-Kerr couplings, there is a common factor $\partial_\delta^4 \mathcal{E}_{\text{arm}}$, so that the null point still exists at the external magnetic bias to let $\partial_\delta^4 \mathcal{E}_{\text{arm}} = 0$.

However, as we increase the stray inductance α, which effectively decreases the inductance ratio β, it causes the ground state to be more unstable. Adding to it, increasing α causes the null point to shift from $\varphi_{\text{ext}} = 2\pi$ to higher magnetic bias. At a relatively large α, the null point may end up in the unstable regime and become unreachable in real experiments. In Fig. 12, we plot the ground-state stability diagram as we change external magnetic flux and α, we further plot shifting of the nulling points as we change α [green curve in Fig. 12]. In Fig. 12, we set the JRM inductance ratio $\beta = 4.0$ and when $\alpha \sim 0.4$, the null point hits the boundary of the unstable regime, which means the null point does not exist in the experiment any longer.

[1] A. A. Clerk, M. H. Devoret, S. M. Girvin, F. Marquardt, and R. J. Schoelkopf, Introduction to quantum noise, measurement, and amplification, Rev. Mod. Phys. **82**, 1155 (2010).

[2] W. H. Louisell, A. Yariv, and A. E. Siegman, Quantum fluctuations and noise in parametric processes. I. Phys. Rev. **124**, 1646 (1961).

[3] J. P. Gordon, W. H. Louisell, and L. R. Walker, Quantum fluctuations and noise in parametric processes. II, Phys. Rev. **129**, 481 (1963).

[4] C. M. Caves, Quantum limits on noise in linear amplifiers, Phys. Rev. D **26**, 1817 (1982).

[5] M. A. Castellanos-Beltran and K. W. Lehnert, Widely tunable parametric amplifier based on a superconducting quantum interference device array resonator, Appl. Phys. Lett. **91**, 083509 (2007).

[6] M. A. Castellanos-Beltran, K. D. Irwin, G. C. Hilton, L. R. Vale, and K. W. Lehnert, Amplification and squeezing of quantum noise with a tunable josephson metamaterial, Nat. Phys. **4**, 929 (2008).

[7] T. Yamamoto, K. Inomata, M. Watanabe, K. Matsuba, T. Miyazaki, W. D. Oliver, Y. Nakamura, and J. S. Tsai, Flux-driven Josephson parametric amplifier, Appl. Phys. Lett. **93**, 042510 (2008).

[8] N. Bergeal, F. Schackert, M. Metcalfe, R. Vijay, V. E. Manucharyan, L. Frunzio, D. E. Prober, R. J. Schoelkopf, S. M. Girvin, and M. H. Devoret, Phase-preserving amplification near the quantum limit with a Josephson ring modulator, Nature (London) **465**, 64 (2010).

[9] N. Bergeal, R. Vijay, V. E. Manucharyan, I. Siddiqi, R. J. Schoelkopf, S. M. Girvin, and M. H. Devoret, Analog information processing at the quantum limit with a Josephson ring modulator, Nat. Phys. **6**, 296 (2010).

[10] M. Hatridge, R. Vijay, D. H. Slichter, J. Clarke, and I. Siddiqi, Dispersive magnetometry with a quantum limited squid parametric amplifier, Phys. Rev. B **83**, 134501 (2011).

[11] N. Roch, E. Flurin, F. Nguyen, P. Morfin, P. Campagne-Ibarcq, M. H. Devoret, and B. Huard, Widely Tunable, Nondegenerate Three-Wave Mixing Microwave Device Operating Near the Quantum Limit, Phys. Rev. Lett. **108**, 147701 (2012).

[12] R. Vijay, D. H. Slichter, and I. Siddiqi, Observation of Quantum Jumps in a Superconducting Artificial Atom, Phys. Rev. Lett. **106**, 110502 (2011).

[13] J. E. Johnson, C. Macklin, D. H. Slichter, R. Vijay, E. B. Weingarten, J. Clarke, and I. Siddiqi, Heralded State Preparation in a Superconducting Qubit, Phys. Rev. Lett. **109**, 050506 (2012).

[14] C. Eichler, D. Bozyigit, and A. Wallraff, Characterizing quantum microwave radiation and its entanglement with superconducting qubits using linear detectors, Phys. Rev. A **86**, 032106 (2012).

[15] A. Metelmann and A. A. Clerk, Quantum-Limited Amplification Via Reservoir Engineering, Phys. Rev. Lett. **112**, 133904 (2014).

[16] L. Spietz, K. Irwin, and J. Aumentado, Superconducting quantum interference device amplifiers with over 27 GHz of gain-bandwidth product operated in the 4–8 GHz frequency range, Appl. Phys. Lett. **95**, 092505 (2009).

[17] T. C. Chien, O. Lanes, C. Liu, X. Cao, P. Lu, S. Motz, G. Liu, D. Pekker, and M. Hatridge, Multiparametric amplification and qubit measurement with a Kerr-free Josephson ring modulator, arXiv:1903.02102 [Phys. Rev. A (to be published)].

[18] A. Metelmann and A. A. Clerk, Nonreciprocal Photon Transmission and Amplification Via Reservoir Engineering, Phys. Rev. X **5**, 021025 (2015).

[19] Q. Zhong, S. K. Ozdemir, A. Eisfeld, A. Metelmann, and R. El-Ganainy, Exceptional Points-Based Optical Amplifiers, Phys. Rev. Appl. **13**, 014070 (2020).

[20] A. Kamal, A. Marblestone, and M. Devoret, Signal-to-pump back action and self-oscillation in double-pump Josephson parametric amplifier, Phys. Rev. B **79**, 184301 (2009).

[21] B. Abdo, A. Kamal, and M. Devoret, Nondegenerate three-wave mixing with the Josephson ring modulator, Phys. Rev. B **87**, 014508 (2013).

[22] C. Eichler and A. Wallraff, Controlling the dynamic range of a Josephson parametric amplifier, EPJ Quantum Tech. **1**, 2 (2014).

[23] B. A. Kochetov and A. Fedorov, Higher-order nonlinear effects in a Josephson parametric amplifier, Phys. Rev. B **92**, 224304 (2015).

[24] G. Liu, T.-C. Chien, X. Cao, O. Lanes, E. Alpern, D. Pekker, and M. Hatridge, Josephson parametric converter saturation and higher order effects, Appl. Phys. Lett. **111**, 202603 (2017).

[25] N. E. Frattini, V. V. Sivak, A. Lingenfelter, S. Shankar, and M. H. Devoret, Optimizing the Nonlinearity and Dissipation of a SNAIL Parametric Amplifier for Dynamic Range, Phys. Rev. Appl. **10**, 054020 (2018).

[26] A. Roy and M. Devoret, Quantum-limited parametric amplification with Josephson circuits in the regime of pump depletion, Phys. Rev. B **98**, 045405 (2018).

[27] D. M. Pozar, *Microwave Engineering*, 4th ed. (Wiley, New York, 2011).

[28] S. Khan, A. Metelmann, and H. Türeci, Quantum nonlinear dynamics of non-degenerate parametric amplification beyond the stiff-pump approximation, APS March Meeting Abstracts (2019), Section V28.007.

[29] N. E. Frattini, U. Vool, S. Shankar, A. Narla, K. M. Sliwa, and M. H. Devoret, Three-wave mixing Josephson dipole element, Appl. Phys. Lett. **110**, 222603 (2017).

[30] V. V. Sivak, N. E. Frattini, V. R. Joshi, A. Lingenfelter, S. Shankar, and M. H. Devoret, Kerr-Free Three-Wave Mixing in Superconducting Quantum Circuits, Phys. Rev. Appl. **11**, 054060 (2019).

[31] V. V. Sivak, S. Shankar, G. Liu, J. Aumentado, and M. H. Devoret, Josephson Array Mode Parametric Amplifier, Phys. Rev. Appl. **13**, 024014 (2020).

[32] L. Spietz, K. Irwin, M. Lee, and J. Aumentado, Noise performance of lumped element direct current superconducting quantum interference device amplifiers in the 4–8 GHz range, Appl. Phys. Lett. **97**, 142502 (2010).

[33] J. Y. Mutus, T. C. White, E. Jeffrey, D. Sank, R. Barends, J. Bochmann, Y. Chen, Z. Chen, B. Chiaro, A. Dunsworth, J. Kelly, A. Megrant, C. Neill, P. J. J. O'Malley, P. Roushan, A. Vainsencher, J. Wenner, I. Siddiqi, R. Vijay, A. N. Cleland, and J. M. Martinis, Design and characterization of a lumped element single-ended superconducting microwave parametric amplifier with on-chip flux bias line, Appl. Phys. Lett. **103**, 122602 (2013).

[34] X. Zhou, V. Schmitt, P. Bertet, D. Vion, W. Wustmann, V. Shumeiko, and D. Esteve, High-gain weakly nonlinear flux-modulated Josephson parametric amplifier using a SQUID array, Phys. Rev. B **89**, 214517 (2014).

[35] O. Naaman, D. G. Ferguson, and R. J. Epstein, High saturation power Josephson parametric amplifier with GHz bandwidth, arXiv:1711.07549 [physics.ins-det].

[36] B. Abdo, F. Schackert, M. Hatridge, C. Rigetti, and M. Devoret, Josephson amplifier for qubit readout, Appl. Phys. Lett. **99**, 162506 (2011).

[37] C. Macklin, K. O'Brien, D. Hover, M. E. Schwartz, V. Bolkhovsky, X. Zhang, W. D. Oliver, and I. Siddiqi, A near–quantum-limited Josephson traveling-wave parametric amplifier, Science **350**, 307 (2015).

[38] T. C. White, J. Y. Mutus, I.-C. Hoi, R. Barends, B. Campbell, Y. Chen, Z. Chen, B. Chiaro, A. Dunsworth, E. Jeffrey, J. Kelly, A. Megrant, C. Neill, P. J. J. O'Malley, P. Roushan, D. Sank, A. Vainsencher, J. Wenner, S. Chaudhuri, J. Gao, and J. M. Martinis, Traveling wave parametric amplifier with Josephson junctions using minimal resonator phase matching, Appl. Phys. Lett. **106**, 242601 (2015).

[39] A. B. Zorin, Josephson Traveling-Wave Parametric Amplifier with Three-Wave Mixing, Phys. Rev. Appl. **6**, 034006 (2016).

[40] Throughout our paper, we make the assumption that the JRM circuit is symmetric; that is, all four inner inductors are identical and all four Josephson junctions are identical.

[41] To be more accurate, we directly solve $\varphi_a^{(3)} = \epsilon \varphi_a^{(1)}$ without high-gain assumption for the perturbation curves in Fig. 3.

[42] L. Ranzani and J. Aumentado, Graph-based analysis of nonreciprocity in coupled-mode systems, New J. Phys. **17**, 023024 (2015).

[43] K. M. Sliwa, M. Hatridge, A. Narla, S. Shankar, L. Frunzio, R. J. Schoelkopf, and M. H. Devoret, Reconfigurable Josephson Circulator/Directional Amplifier, Phys. Rev. X **5**, 041020 (2015).